

The opposition effect in Saturn's main rings as seen by Cassini ISS: 4. Correlations of the surge morphology with surface albedos and VIMS spectral properties



Estelle Déau^{a,b,*}, Luke Dones^c, Michael I. Mishchenko^d, Robert A. West^a, Paul Helfenstein^e, Matt M. Hedman^f, Carolyn C. Porco^g

^aNASA Jet Propulsion Laboratory, Pasadena, CA, United States

^bUniversity of California, Los Angeles, CA, United States

^cSouthwest Research Institute, Boulder, CO, United States

^dNASA Goddard Institute for Space Studies, New York, NY, United States

^eCornell University, Ithaca, NY, United States

^fUniversity of Idaho, Moscow ID, United States

^gSpace Science Institute, Boulder CO, United States

ARTICLE INFO

Article history:

Received 23 May 2017

Revised 4 December 2017

Accepted 18 December 2017

Available online 29 December 2017

ABSTRACT

In this paper, we continue our analysis of the saturnian ring opposition effect seen by Cassini ISS. The ring opposition effect is a peak in the rings' reflectivity caused as the directions from a spot on the rings to the observer and to the light source, respectively, converge toward zero degrees. So far, the exact origin of the ring's opposition effect is still a matter of debate. In our previous work (Déau, et al., 2013, *Icarus*, 226, 591–603), we compared the opposition effect morphology with the rings' optical depth and found that only the slope of the linear part of the rings' phase curves was strongly correlated with the optical depth. We interpreted this as an indication of the predominant role of interparticle shadowing at moderate phase angles ($\alpha \sim 10\text{--}40^\circ$). More recently (Déau, 2015, *Icarus*, 253, 311–345), we showed that interparticle shadowing cannot explain the behavior at low phase angles ($\alpha < 1^\circ$), indirectly confirming our 2013 result. These findings led to the idea that coherent backscattering is preponderant at the smallest phase angles. Coherent backscattering depends on the microscopic scale of the regolith, and there is a growing body of evidence that regolith grain size, porosity, roughness, and composition control the opposition surge behavior for $\alpha < 1^\circ$. To test this hypothesis, we compare the opposition surge morphology to the regolith albedo and other spectral properties related to the regolith, such as water ice band depths and spectral slopes derived from Cassini VIMS data (Hedman et al., 2013, *Icarus*, 223, 105–130). Indeed, it has been recently proven that coherent backscattering affects the water ice band depth variations with phase angle for icy saturnian regoliths (Kolokolova et al., 2010, *The Astrophysical Journal Letters*, 711, L71–L74). We find that the opposition surge morphology is strongly correlated with the water ice band depth and the regolith albedo. We interpret this finding as an indication that coherent backscattering plays a role in affecting both the water ice band depths and the opposition surge at low phase angles ($\alpha < 1^\circ$). As the regolith albedo and spectral properties are related to the grain size, porosity, roughness, and composition, we try to assess which of these regolith properties are preponderant in coherent backscattering. Our study is able to narrow down the parameter space of these properties, whose values allow a good match between the angular width predicted by models of coherent backscattering and the width of the observed peak.

Published by Elsevier Inc.

1. Introduction

The ring opposition effect is a surge in ring brightness that occurs as the alignment of the observer, the rings, and the Sun converges on zero degrees. Despite numerous studies on the opposition effect in Saturn's rings (Müller, 1885; 1893; Seeliger,

* Corresponding author at: NASA Jet Propulsion Laboratory, 4800 Oak Grove Drive Pasadena CA 91107 United States.

E-mail address: deau@jpl.nasa.gov (E. Déau).

1884; 1887; Lyot, 1929; Kawata and Irvine, 1974; Lumme and Irvine, 1976; Esposito, 1979; Esposito et al., 1979; Muinonen, 1990; Mishchenko, 1992; 1993; Poulet et al., 2002; Salo and Karjalainen, 2003; Mishchenko et al., 2006; Nelson et al., 2006; Altobelli et al., 2007; French et al., 2007; Porco et al., 2008; Mishchenko and Dlugach, 2009; Salo and French, 2010; Déau et al., 2013a; Déau, 2015; Déau et al., 2018a), its origin remains unresolved. The discovery of the phenomenon (Müller, 1885; 1893; Seeliger, 1884; 1887) has recently been followed by a new generation of studies, which were more quantitative and based on accurate observations and theoretical models. These have greatly improved our knowledge of the opposition effect's behavior: for each ring (Lumme and Irvine, 1976; Poulet et al., 2002; French et al., 2007; Salo and French, 2010), within each ring (Poulet et al., 2002; French et al., 2007; Déau et al., 2013a), with wavelength (Franklin and Cook, 1965; Lumme and Irvine, 1976; Esposito et al., 1979; Poulet et al., 2002; French et al., 2007; Salo and French, 2010; Déau et al., 2013a), with the polarization of light (Lyot, 1929; Johnson et al., 1980; Mishchenko, 1993; Dollfus, 1996; Mishchenko et al., 2006; Mishchenko and Dlugach, 2009), and with Saturn's seasons (Mishchenko and Dlugach, 2009; Salo and French, 2010). These works have used ground-based, Earth-based (Hubble Space Telescope), and spacecraft (Cassini) observations, which are remarkably complementary in terms of phase angle coverage, phase angle sampling, spatial resolution, and wavelength. The combined results from these studies led to the following realizations about the ring opposition effect:

- the bulk of the opposition surge in optical and unpolarized light operates at phase angles less than 2° (Müller, 1885; 1893; Seeliger, 1884; 1887);
- both the brightest main rings (the A and B rings) exhibit an opposition effect (Lumme and Irvine, 1976; Esposito et al., 1979), as do more tenuous ones: the C ring (Poulet et al., 2002; French et al., 2007; Salo and French, 2010; Déau et al., 2013a), the Cassini Division (Poulet et al., 2002; Déau et al., 2013a), the D ring (Déau et al., 2013a), and the E ring (Pang et al., 1983; Larson, 1984; Déau et al., 2009);
- the dimmest main rings (D and C rings, Cassini Division) exhibit the highest and widest opposition peaks (Déau et al., 2013a);
- the ring opposition effect varies with wavelength (Franklin and Cook, 1965; Lumme and Irvine, 1976; French et al., 2007; Salo and French, 2010; Déau et al., 2013a), and the effect is noticeably more pronounced at short and long wavelengths, i.e. the near ultraviolet (French et al., 2007) and the near infrared, respectively (French et al., 2007; Déau et al., 2013a);
- the morphology of the ring opposition effect varies with seasons, i.e. with the solar elevation $|B'|$ (Salo and French, 2010);
- the ring opposition effect is observed in linear and circular polarized light (Lyot, 1929; Mishchenko, 1993; Mishchenko et al., 2006; Mishchenko and Dlugach, 2009) in addition to unpolarized light;
- the opposition effect is observed in the thermal infrared in the C ring (Altobelli et al., 2007), but no similar narrow surge is observed in the A and B rings (Wallis et al., 2005; 2006; Altobelli et al., 2009).

However, none of these findings have led to a solid explanation of the origin of the opposition effect in the saturnian system. Attempts to explain it involve the following physical mechanisms:

- (a) interparticle shadow hiding or mutual shadowing, (see Seeliger, 1887; Kawata and Irvine, 1974; Esposito, 1979; Porco et al., 2008; Salo and French, 2010; Déau, 2015), which consists of shadows of ring particles that are hidden behind the particles when the phase angle is close to zero, and that become apparent at larger phase angles. This mechanism was the *classical* explanation of the ring opposition effect;

- (b) coherent backscattering, see Muinonen (1990); Mishchenko (1993); Mishchenko et al. (2006); Salo and French (2010); Déau (2015), is caused by constructive interference between pair of conjugate electromagnetic waves in a medium of grains (this effect is universally present at any wavelength and any grain size, but the angular width of various manifestations of coherent backscattering up to several tenths of a degree is easily observable when the grain sizes are comparable to the wavelength of light);
- (c) regolith shadow hiding, see Salo and French (2010), Déau (2015), is similar to interparticle shadow hiding; however, it operates at a much smaller scale, i.e., the shadows are those of the regolith grains on top of each ring particle.
- (d) near-field interaction, see Petrova et al. (2007), is caused by the inhomogeneity of waves in the immediate vicinity of grains. Though its contribution should be important mostly for densely-packed, low-albedo media, which is probably not relevant for Saturn's rings, this mechanism is worth mentioning.

Some studies have assumed a single mechanism of the three cited above to explain the whole effect (Seeliger, 1887; Kawata and Irvine, 1974; Esposito, 1979; Mishchenko, 1993; Degiorgio et al., 2010), while others have assumed a combination of the mechanisms (Poulet et al., 2002; Nelson et al., 2006; French et al., 2007; Salo and French, 2010; Déau, 2015). A final group of ring studies has ruled out some of the hypotheses presented above by comparing the predicted trends of the models with observations. In particular, interparticle shadow hiding has been almost unequivocally ruled out as the preponderant mechanism acting in the ring opposition peak (i.e. the opposition effect at very low phase angles). Indeed, it has been claimed that interparticle shadow hiding by identical ring particles requires unphysically small volume densities for Saturn's main rings to reproduce the height of their opposition spike (Lumme et al., 1987; Muinonen, 1990), whereas other rings that are less dense than the main saturnian ones (e.g. E ring, jovian, uranian, and neptunian) do not show higher opposition spikes, even when removing the effect of the finite size of the Sun (Déau et al., 2009). Finally, Déau (2015) demonstrated in detail that models of interparticle shadow hiding, using realistic volume densities from previous studies (Salo and Karjalainen, 2003; Porco et al., 2008), predict heights (or amplitudes) that behave in a completely distinct way from the observations. This point is the latest and most direct proof that interparticle shadow hiding *alone* cannot reproduce the ring opposition effect (Déau, 2015, Fig. 8).

In the meantime, coherent backscattering was also considered as an explanation for the ring opposition effect (Muinonen, 1990; Mishchenko, 1993). However, it is difficult to directly observe coherent backscattering¹ in the laboratory with planetary regolith analogs, meaning that although what is observed is surely backscattering, it is not necessarily *coherent* backscattering, see details in Tishkovets and Mishchenko (2010).² For quite some time, coherent backscattering did not behave as expected in polarized

¹ Direct observations of coherent backscattering in planetary regolith analogs are obtained when a correlation is established between the measured outputs of the phenomenon and the sample properties, as done by Kuga and Ishimaru (1984) or Piatak et al. (2004). In addition, indirect observations of coherent backscattering in regoliths are so far confirmed by strong phase angle variations of color ratio (Shkuratov et al., 1999b), or polarization (Hapke et al., 1993; Nelson et al., 2000; Shkuratov et al., 2002; 2007).

² To that matter, it can be noticed that laboratory experiments and planetary surfaces are not subject to the same illumination conditions (i.e. coherent or non-coherent light source). Indeed, we note that all reports of purported coherent backscattering observed in the laboratory are made with lasers, which produce coherent light. However, sunlight is incoherent (Herman et al., 2014), or at least it is not as coherent as lasers (Mashaal et al., 2012). Still, Shkuratov et al. (1999b) indirectly observed coherent backscattering with incoherent laboratory light sources.

and unpolarized light (Muinonen, 1994), but agreements are now found, see Rosenbush et al. (1997), Mishchenko et al. (2006). Finally, there are heated debates about the correct formalism for treating closely-packed particles, as in a regolith (Shkuratov and Zubko, 2008; Petrova et al., 2008; Tishkovets et al., 2011). These issues have delayed the acceptance of coherent backscattering by the ring photometric community. In short, recent works suggest that the observed opposition effect is a combination of the mechanisms described above (Poulet et al., 2002; Nelson et al., 2006; French et al., 2007; Salo and French, 2010; Déau, 2015); however, many questions remain unanswered. We will focus on a few topics related to the ring opposition effect observed in optical and unpolarized light:

- ① What is the main mechanism involved in the ring opposition surge?
- ② How do the physical properties of the regolith relate to the opposition surge morphology?
- ③ Do the physical properties of the regolith involved in the ring opposition effect significantly vary from ring to ring?

In Part 1 of this study (Déau et al., 2013a, hereafter Paper 1), we investigated the morphology of the opposition effect in the main rings of Saturn, and found a strong correlation between morphological parameters and the optical depth. In Part 2 (Déau, 2015, hereafter Paper 2), we conducted a benchmark study of analytical physical models of the opposition effect, and concluded that the hypothesis of homogeneity (i.e., a single particle size, random spacing of particles, and small volume filling factor) led to invalid results when the outputs were compared to the same physical properties from independent studies. In Part 3 (Déau et al., 2018a, hereafter Paper 3), we isolated the surge angular width and launched an in-depth study of this parameter to test the roles of regolith porosity, ring filling factor, particle size distribution and grain size distribution of Saturn's rings in the opposition surge. In the present study, which constitutes the fourth part, we will look again at the morphology of the ring opposition effect. In Paper 1, we found a strong dependence on the optical depth of the A and B rings, while this dependence was weaker in the C ring and the Cassini Division. In other words, the strength of the optical depth dependence varies from one ring to another. The weak dependence noted in diffuse rings deserves extra attention in order to find its cause. One clue could be the surface albedo. Many studies have related the morphology of the opposition peak to the surface albedo (Helfenstein et al., 1997; Belskaya and Shevchenko, 2000; Shevchenko et al., 2012). We were not able to make this kind of correlation in our previous research because the albedo of Saturn's rings was not determined yet. There were some values derived with the Voyager data in the A and C rings (Cooke, 1991; Dones et al., 1993) but not in the B ring and the Cassini Division. It is only recently that the single scattering albedo was determined in all the main rings (Hedman et al., 2013; Déau and Helfenstein, 2018). Due to the complex nature of Saturn's rings, the albedo can be either:

- macroscopic, when the elementary scatterers of photometric models are assumed to be whole ring particles (Dones et al., 1993). These particles can be as large as 10 m (Zebker et al., 1985; French and Nicholson, 2000; Cuzzi et al., 2009); or
- microscopic, because the mean photon path length of spectroscopic models is less than 30 μm (Hedman et al., 2013), which is about the size of the ring regolith grains (Hedman et al., 2013). Many studies found these grains to have a size of less than 50 μm (Poulet et al., 2002; Déau, 2015; Cuzzi et al., 2009). These small grains are known to exist, at least freely in the

B ring, inducing manifestations called spokes (Doyle and Grun, 1990; McGhee et al., 2005; Mitchell et al., 2013)³

Searching for correlations between morphological parameters and these two types of albedo will bring us valuable clues about which opposition effect mechanism is preponderant. Indeed, interparticle shadowing is a macroscopic mechanism, while regolith shadow hiding and coherent backscattering are intrinsically microscopic.

Finally, to better understand the interplay between the opposition effect mechanisms, we will compare the morphology of the opposition peak of Saturn's rings with the water ice band depths. In the case of the rings, Hedman et al. (2013) found that the spectral properties are only slightly dependent on the geometry. Radial profiles of the spectral properties on the lit side at low phase showed similar shapes to those observed on the lit side at high phase and on the unlit side at low phase. They interpret these findings as an indication that the ring spectral properties at high phase should include a large fraction of light that has interacted multiple times with the ring particles, while the ring spectral properties at low phase angles should primarily involve regolith structure and composition. Correlations or independence of this spectral property with the opposition surge morphology could then help us to identify the common or distinct nature of the scattering acting in the ring opposition effect.

In Section 2, we present the datasets from which we derived the morphological parameters and the spectral properties of the rings of Saturn. We also present the morphological model used. In Section 3, we present our results about the main rings first (Section 3.1), i.e., the comparison of the morphological parameters with the macroscopic and microscopic ring albedos, and with the spectral properties. Second, we present our results on the opposition effect of the main rings as a function of the distance from Saturn (in map form), from the C ring to Enceladus. Our map is compared to the maps of water ice band depths and spectral slopes. In Section 4, we discuss the role of the mechanisms on the opposition effect morphology, and bring new clues to the predominance of the mechanisms involved in the ring opposition effect. In Section 5, we give our main conclusions.

2. Methodology

2.1. The opposition effect morphology using ISS data

2.1.1. Morphological models

Our previous works on the morphology of the opposition effect in Saturn's rings (see Paper 1) and other planetary surfaces (Déau et al., 2009; 2016; 2018b) describe the morphological models we employ for the opposition effect. Here, we simply retrieve the values of the morphological parameters of the opposition surge from Paper 1. But for completeness, and also because of the diversity of morphological models, we provide a brief description of the models we have used in Paper 1.

Our first morphological model is the linear-by-parts model. First introduced by Lumme and Irvine (1976), it is very convenient for the ISS ring data because the variations in phase angle sampling and range (see Paper 1) are not well managed with other morphological models (see Déau 2007, Fig. F.2, p. 371). In Paper 1, before using this model, we corrected the ISS radiance factor data (I/F) with the Chandrasekhar (1960) inversion to $\tau_0 p(\alpha)$ (where τ_0 is

³ In theory, there should not be a strong separation between microscopic and macroscopic scales since photometry may be defined by the whole vertical extent of the regolith layer with larger grains dominating the deeper layers, whereas coherent backscattering can be produced by the outer layer dominated by microscopic grains. The latter cause the spokes when they get levitated, e.g. (McGhee et al., 2005).

Indeed, that temporal incoherence doesn't matter in producing coherent backscattering. See the paragraph preceding Section 18.3, p. 277 in Mishchenko (2014).

the average single scattering albedo that is referred to the “ring bulk albedo”, see Déau and Helfenstein (2018) and Section 3.1, and $p(\alpha)$ is the average single scattering function, meaning that multiple scattering is explicitly assumed to be insignificant):

$$\varpi_0 p(\alpha) = \frac{I}{F} \cdot \frac{4(\mu + \mu_0)}{\mu_0} \cdot \left(1 - e^{-\tau\left(\frac{1}{\mu} + \frac{1}{\mu_0}\right)}\right)^{-1} \quad (1)$$

with μ and μ_0 are the cosine of the incidence and emergence angles, and τ is the normal optical depth from the Voyager PPS (Lane et al., 1982). Please note the typo in Eq. (1) of Paper 1 and read I/F instead of $1/F$.

The equations of the linear-by-parts model are:

$$r_{lin}(\alpha < 0.3^\circ) = -A_0 \cdot \alpha + B_0 \quad (2)$$

$$r_{lin}(\alpha > 1.5^\circ) = -A_1 \cdot \alpha + B_1, \quad (3)$$

where r_{lin} is the ring reflectivity ($r_{lin} = \varpi_0 p(\alpha)$), and A_0 , B_0 , A_1 , B_1 are the coefficients of the linear functions (all assumed to be positive). The coefficients from both fits then provide A , HWHM and S , which are defined as follows:

$$A = \frac{B_0}{B_1}, \quad (4)$$

$$\text{HWHM} = \frac{(B_0 - B_1)}{2(A_0 - A_1)}, \quad (5)$$

$$S = -A_1. \quad (6)$$

The surge amplitude A is dimensionless. The Half Width at Half Maximum (HWHM) of the surge is given in degrees, and the absolute slope S is in ring reflectivity unit per degree of phase angle. To estimate the error bars, we use the propagation of errors method of Déau et al. (2013b). We obtain:

$$\Delta A = \left[\left(\frac{\Delta B_0}{B_1} \right)^2 + \left(\frac{B_0}{B_1^2} \times \Delta B_1 \right)^2 \right]^{1/2} \quad (7)$$

$$\Delta \text{HWHM} = \left[\left(\frac{\Delta B_0}{2(A_0 - A_1)} \right)^2 + \left(\frac{\Delta B_1}{2(A_0 - A_1)} \right)^2 + \left(\frac{(B_0 - B_1)}{2(A_0 - A_1)^2} \right)^2 \times (-(\Delta A_0)^2 + (\Delta A_1)^2) \right]^{1/2} \quad (8)$$

$$\Delta S = \Delta A_1, \quad (9)$$

where ΔA_0 , ΔA_1 , ΔB_0 , ΔB_1 are the $1-\sigma$ uncertainty estimates returned by the procedure `linfit.pro` of IDL (Interactive Data Language, see <http://www.harrisgeospatial.com/idl/>).

Another model used in Paper 1 was the logarithmic model of Bobrov (1970). To use this model, the radiance factor data (in $\varpi_0 p(\alpha)$) is fit with a logarithmic function:

$$r_{log}(\alpha) = a_0 + a_1 \cdot \ln(\alpha), \quad (10)$$

where r_{log} is the ring reflectivity ($r_{log} = \varpi_0 p(\alpha)$).

2.1.2. Dataset for Saturn's main rings

In this paper, we did not process any ISS data, but we retrieved the morphological parameters from Paper 1. These values were obtained by using ISS images containing the opposition spot ($\alpha < 2.5^\circ$), and images at larger phase angles ($\alpha < 25^\circ$) to track the tail of the surge (the list is given in Table 2 of Paper 1). In Paper 1, we used both ISS images of the narrow angle camera and wide

angle camera (NAC and WAC) with the CLEAR filters (wavelength $\lambda = 0.611 \pm 0.170 \mu\text{m}$ for the NAC and $\lambda = 0.635 \pm 0.143 \mu\text{m}$ for the WAC, see Table 1 of Paper 1). The images containing the opposition spot are mostly located in the C ring and the B ring, with a few in the Cassini Division and the A ring, meaning that the resulting phase curves do not have the same phase angle coverage. This latter point will be discussed in Section 4.2.6.

In the first step, we applied the Chandrasekhar (1960) inversion (see Eq. (1) in Paper 1) to take into account the slight change in viewing geometry from one image to another. Examples of these phase curves for the A, B, and C rings and the Cassini Division are given in Fig. 1a. The curves in Fig. 1a are presented normalized to the overall median of the points to appreciate the morphology of the different surges, without considering the albedo corresponding to each curve.

In the second step, we fit the opposition curves with a morphological model. As stated above, we used the linear-by-parts model. However, we also performed a fit with the logarithmic model, as it fits the overall shape of the phase curves well. Examples are given in Fig. 1b. In this figure, one can see that the B ring has the smallest and narrowest peak. To quantify this statement, we used another morphological model. The linear-by-parts model allowed us to derive the amplitude A of the opposition peak and the width at half maximum HWHM.

The retrieved morphological parameters from Paper 1 are represented as a function of the distance to Saturn in Fig. 2. Before doing cross-comparison with these parameters in the following sections, we propose a brief description of the values with distance to Saturn.

In panels a and b of Fig. 2, one can easily see that the B ring has the smallest and narrowest peaks, in quantitative agreement with Fig. 1b.

As reported in Paper 1, the variations of the amplitude and width provide similar trends with respect to the distance to Saturn: there is a decrease from the C ring to the B ring, then an increase is observed in the Cassini Division. In the Cassini Division, points are widely scattered; however, there is a continuity between the B ring, the Cassini Division and the A ring. Finally, in the A ring, we note an increase from its inner part to its middle part. A lack of data did not allow us to determine the surge parameters for the outer part of the A ring (see Paper 1), so we cannot conclude whether the observed increase would have continued in the outer A ring. By contrast, the slope was derived for the outer part of the A ring in Paper 1. Interestingly, we observe that the changes in the slope with distance to Saturn are very different: the values of the A and B rings are continuous with each other, but are not connected with those of the Cassini Division (see Fig. 2c).

2.2. The spectral properties using VIMS data

Recently, Déau et al. (2016) showed that a relationship exists between the surge amplitude and the near-infrared spectral slope for powdered meteorite samples. For both properties, they found that their behavior changes at a reflectance (at $\alpha = 5^\circ$) of ~ 0.08 . This result was interpreted as a strong indication of the role of the microscopic properties of the meteorite samples in forming the opposition effect. Planetary rings are not like meteorite powders; however, there is a growing body of evidence that the ring opposition effect involves the regolith of ring particles. Indeed, the work of Salo and French (2010) showed that a significant part of the ring opposition effect was due to the regolith (particularly the narrow part of the surge), while a smaller part (governed by interparticle shadow hiding) contributes to the broad surge. As a result, even though planetary rings are not similar to meteorite samples, if we seek to understand the regolith, it is legitimate to follow a similar methodology, i.e., comparing the opposition surge morphology to

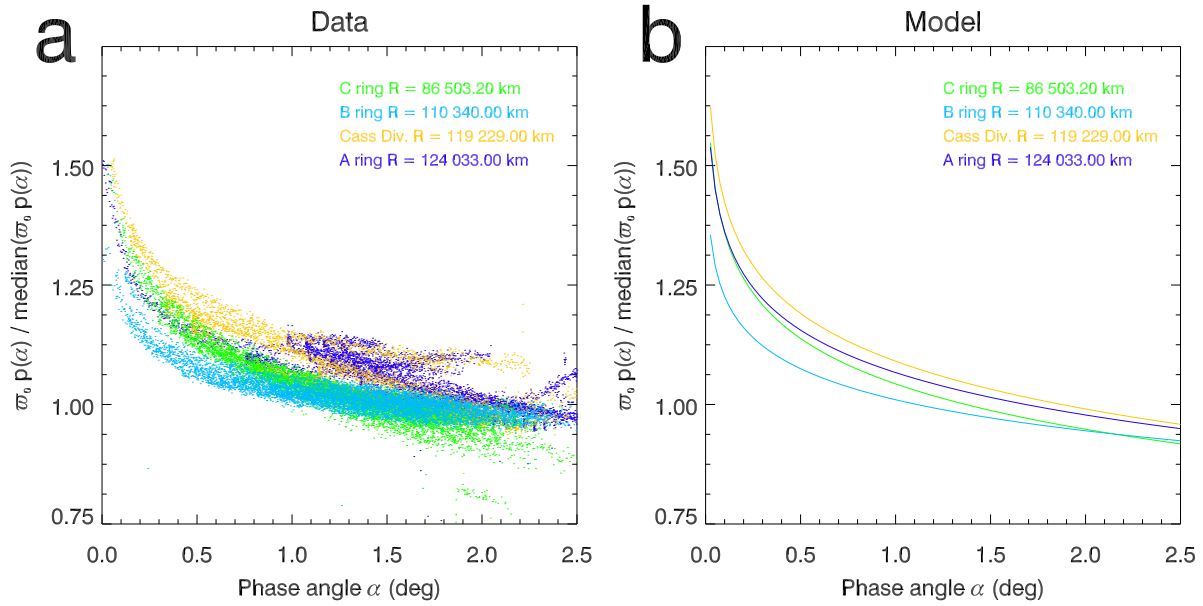


Fig. 1. Left: The phase curves of four representative regions of Saturn's main rings (distances to Saturn's center are indicated) using Cassini ISS data. The data, originally in I/F , were converted to $\varpi_0 p(\alpha)$ using the inversion of Chandrasekhar (1960), see Eq. (1). They are all normalized with their own median to ease comparison between the curves. Right: Fit phase curves using the logarithmic model of Bobrov (1970).

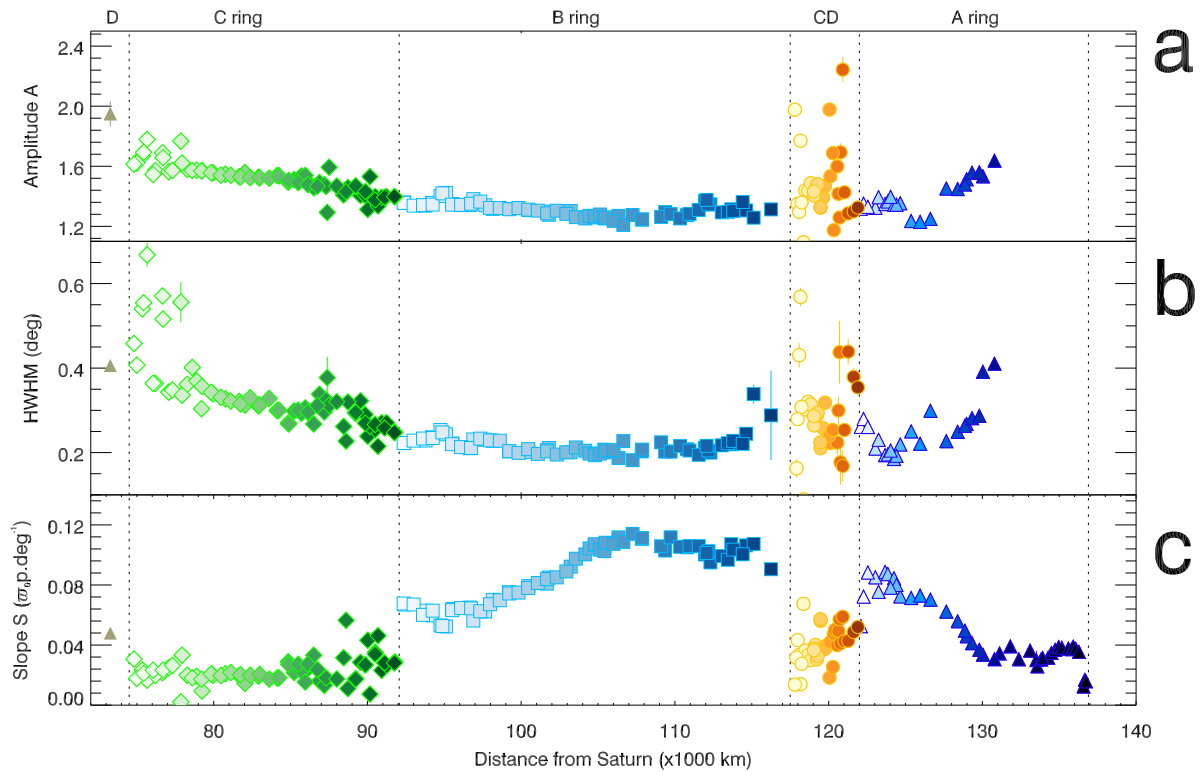


Fig. 2. Retrieved morphological parameters of the opposition surge from Paper 1 using the linear-by-parts model (top: Amplitude A , middle: angular width HWHM, bottom: Slope S) as a function of radial distance. Symbol shapes correspond to different rings. Shading of colors (from fainter to darker) is introduced to represent increasing distance from Saturn. The error bars are given, and are in most cases smaller than the symbols' size. (For interpretation of the references to color in this figure legend, the reader is referred to the web version of this article).

the spectral properties for Saturn's rings. This is also why we have favored the VIMS datasets for the ring spectral properties, instead of the color ratios from the ISS data, which would have been easier for us to obtain.

The VIMS observations that we have retrieved from Hedman et al. (2013) and Filacchione et al. (2012) were acquired during the VIMS_008_RI_RDHRCOMP (20–21 May 2005)

and VIMS_036_RI_SUBML001 observations (19–20 December 2007), respectively.

For the VIMS_008_RI_RDHRCOMP observation, the solar phase angle was between 12.7 and 41.1° , the solar elevation angle was -21.6° , and the spatial resolution was $44\text{--}51 \text{ km.pixel}^{-1}$ for the VIS channel and $131\text{--}154 \text{ km.pixel}^{-1}$ for the IR channel. For the VIMS_036_RI_SUBML001 observation, the solar phase an-

gle was about 29° , the solar elevation was -12° , and the spatial resolution was about $112 \text{ km.pixel}^{-1}$ for the VIS channel and $170\text{--}340 \text{ km.pixel}^{-1}$ for the IR channel.

Here, we retain as spectral properties five parameters that describe the variations of brightness with wavelength:

- The water ice band depths (at $1.25 \text{ }\mu\text{m}$, $1.5 \text{ }\mu\text{m}$, and $2.0 \text{ }\mu\text{m}$) were calculated using the formula:

$$BD_\lambda = \frac{I/F_{\text{cont}} - I/F_{\text{band}}}{I/F_{\text{cont}}}, \quad (11)$$

where I/F_{band} is the brightness in the middle of the chosen band (either 1.25 , 1.5 , or $2.0 \text{ }\mu\text{m}$), and I/F_{cont} is a continuum brightness level inferred from regions outside the band.

- The other important microscopic signatures that can be extracted from VIMS are the spectral slopes. These slopes were calculated using the formula:

$$S_{\lambda_1-\lambda_2} = \frac{I/F_{\lambda_2} - I/F_{\lambda_1}}{(\lambda_2 - \lambda_1) \times I/F_{\lambda_2}}, \quad (12)$$

where I/F_{λ_1} and I/F_{λ_2} are the brightnesses at wavelengths λ_1 and λ_2 , respectively. Filacchione et al. (2012) and Hedman et al. (2013) have defined two slopes: one in the near ultraviolet ($\lambda_1 = 0.35 \text{ }\mu\text{m}$ and $\lambda_2 = 0.55 \text{ }\mu\text{m}$), usually called the blue slope (S_{NUV}), and one in the near infrared ($\lambda_1 = 0.55 \text{ }\mu\text{m}$ and $\lambda_2 = 0.95 \text{ }\mu\text{m}$), usually called the red slope (S_{NIR}).

While both datasets are similar, the radial resolution is better for VIMS_008_RI_RDHRCOMP. As a result, for the rest of the paper, we will compare the ISS data to the spectral properties of this VIMS observation.

Note that the water ice band depths are calculated in the near infrared, while the spectral slopes cover the visible as well as a part of the near ultraviolet and the near infrared. Our ISS data were taken in the visible, which means that comparing the opposition surge with spectral properties will be done regardless of the wavelength domain of each property. The goal of this methodology is to seek correlations between the surge morphology and the spectral properties of the regolith, which are believed to be microscopic markers of the composition, and the mechanical properties of the regolith (grain size, porosity, and roughness). This will be detailed in the following section.

3. Results

3.1. Variations of A and HWHM with bulk albedo and regolith albedo

In previous work about the main rings' surge morphology (Poulet et al., 2002; French et al., 2007; Salo and French, 2010; Déau et al., 2013a), there is no direct comparison of the resulting morphological parameters with the albedo. However, by comparing the morphological parameters of the previously cited works to the single scattering albedo (ϖ_0) derived using the Hapke model in some of these studies, we can infer the major trends. First, we emphasize that all these studies agree that the single scattering albedo increases from the C ring and the Cassini Division to the A ring and B ring. In order to present the findings of Poulet et al. (2002), French et al. (2007), Salo and French (2010), we will use this order, since it represents increasing ϖ_0 . The results of Poulet et al. (2002) show a decrease of A and HWHM for the C ring and the Cassini Division to the A ring, and then a plateau from the A ring to the B ring at $0.555 \text{ }\mu\text{m}$, while a slight increase is noted from the A ring to the B ring at $0.336 \text{ }\mu\text{m}$. French et al. (2007) partially agree with these findings (the decrease from the C ring to the A ring), but found a decrease from the A ring to the B ring at both wavelengths.

In the present study, we did not calculate a single scattering albedo value from our opposition phase curves because the single scattering albedo ϖ_0 cannot be accurately obtained with data having a restricted phase angle coverage. As an example to illustrate our statement, Poulet et al. (2002) obtained $\varpi_0 = 0.90 \pm 0.07$ at $0.555 \text{ }\mu\text{m}$ in the B ring, similar to the result of French et al. (2007) ($\varpi_0 = 0.89 \pm 0.02$ at $0.555 \text{ }\mu\text{m}$), which demonstrates that the agreement of their results is independent of the Hapke model used. (Poulet et al. (2002) used the Hapke (1984, 1986a) model, whereas French et al. (2007) used the Hapke (1984, 1993, 2002) model). However, most recent studies found smaller single scattering albedo values (Déau and Helfenstein, 2018; Hedman et al., 2013), suggesting that the Hapke model overestimates the single scattering albedo from the limited range of phase angles available in Earth-based observations ($\alpha \leq 6^\circ$), see also Cuzzi et al. (2017). Then, we use two kinds of albedo:

- Macroscopic, defined as the albedo of a patch of an ensemble of ring particles, see the study of Déau and Helfenstein (2018). This albedo is uncorrected from Saturnshine and self-gravity wakes, and is referred as “bulk” albedo. It was derived using the Hapke (1984, 1986a) model on almost complete ISS phase curves ($0.01^\circ \leq \alpha \leq 178.9^\circ$) in CLEAR filters ($\lambda = 0.611 \pm 0.170 \text{ }\mu\text{m}$ for the NAC and $\lambda = 0.635 \pm 0.143 \text{ }\mu\text{m}$ for the WAC, see Table 1 of Paper 1).
- microscopic, when considering the albedo of the tiny grains on top of each ring particle, see the study of Hedman et al. (2013). This microscopic albedo (also referred as regolith albedo) was derived by applying the spectral model of Shkuratov et al. (1999a) to the VIMS radial profile VIMS_008_RI_RDHRCOMP (at $12.7\text{--}41.1^\circ$ of phase angle), containing spectra from 0.35 to $5.2 \text{ }\mu\text{m}$. The microscopic albedo $A_{1.13}$ was derived at $1.13 \text{ }\mu\text{m}$, see Hedman et al. (2013, Fig. 27), but belongs to an ensemble that was calculated at wavelengths between 0.35 and $5.2 \text{ }\mu\text{m}$. We choose to retain the value at $1.13 \text{ }\mu\text{m}$ as a reference to Hedman et al. (2013).

We now present our results as a function of these two ring albedos in Fig. 3. In Fig. 3a, the morphological parameter A is presented as a function of the bulk macroscopic albedo ϖ_0 , while in Fig. 3b, it is presented as a function of the regolith (microscopic) albedo $A_{1.13}$. For now, we focus on the morphological parameters of the surge, because these parameters were not as strongly correlated with the optical depth as the slope S was, see Paper 1. We will present the slope variations in Section 3.3.

When comparing the surge morphological parameters to the albedo ϖ_0 and $A_{1.13}$, we find three major trends. First, the trends of the amplitude and the HWHM are almost identical (see Fig. A.1). Since both parameters vary the same way (as noted in Fig. 2), it implies that A and HWHM are likely to be controlled by the same mechanisms, though we will return to this assumption in Section 5. Finally, we note that the error bars are larger with HWHM than with A . This is because A is always retrieved with smaller error bars since it is a simple ratio, see Déau et al. (2013b).

Second, both A and HWHM unambiguously decrease with increasing bulk or regolith albedo, in agreement with the qualitative findings of French et al. (2007). No plateau or slight increase from the A ring to the B ring is observed with our data, contrary to Poulet et al. (2002). We attribute these marginal behaviors to the poor phase angle sampling of the phase curves of Poulet et al. (2002), since the results of French et al. (2007) from data having a better phase angle sampling and a wider phase angle coverage do match our trend.

Third, we note that the strength of the correlation between A (or HWHM) and the albedo depends on whether the albedo is macroscopic or microscopic. In the macroscopic case, the relationship between A and the bulk albedo is less defined, as illus-

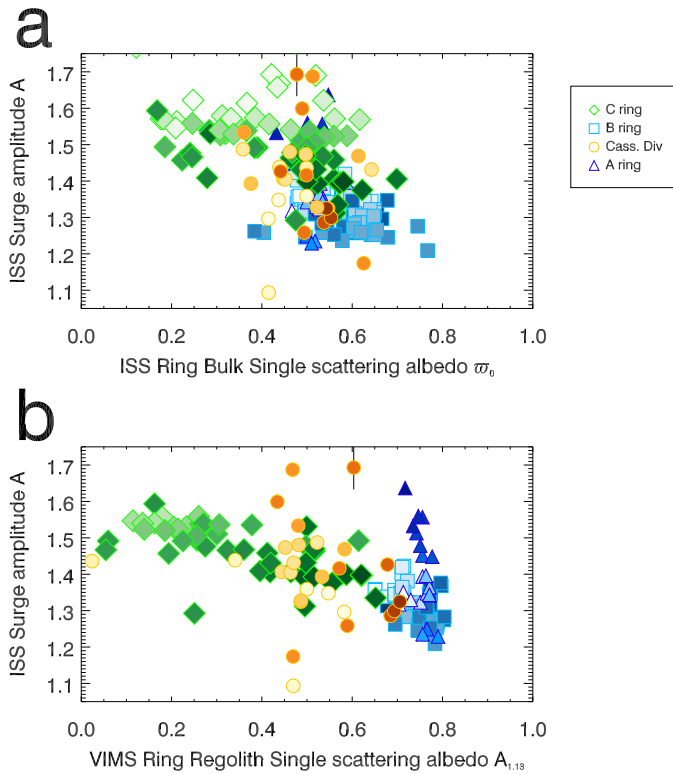


Fig. 3. Amplitude of the surge A in Saturn's main rings presented as a function of the albedo. In panel a, A is given as a function of the bulk (or macroscopic) albedo ω_0 derived from ISS data by Déau and Helfenstein (2018), and in panel b, A is given as a function of the regolith (or microscopic) albedo $A_{1,13}$ derived from VIMS data by Hedman et al. (2013). Symbol shapes correspond to different rings. Shading of colors (from fainter to darker) represents increasing distance to Saturn, see Fig. 2. (For interpretation of the references to color in this figure legend, the reader is referred to the web version of this article).

trated by a large scatter in the (A, ω_0) parameter space, see Fig. 3a. The same trend is noted in the (HWHM, ω_0) parameter space. We can conclude that the morphological parameters of the surge are poorly correlated with the bulk albedo. By contrast, in the case of the regolith albedo, the relationship is roughly linear (for example, a linear fit in the C ring leads to a correlation coefficient of -71.5% in Fig. 3b, against -33.8% in Fig. 3a), so it can be noted that there is somewhat less scatter than for the bulk albedo case. This quasi-linear relationship allows us to conclude that A and HWHM are strongly correlated with the regolith albedo. There exist some scattered points in the Cassini Division and the A ring in Fig. 3b, which slightly weakens the strong correlation between A (or HWHM) and $A_{1,13}$; however, they only represent a small fraction of the data points. For HWHM, these points are associated with the largest error bars.

Finally, we report two minor trends. The first one can be noticed using the color code in Fig. 3. We note that the outer C ring (known as the C ring ramp) is very close to the inner B ring regions in the $(A, A_{1,13})$ parameter space, and the outer Cassini Division (known as the Cassini Division ramp) is also very close to the inner A ring regions. While these ring boundaries exhibit strong variations in optical depth profiles (Colwell et al., 2009), they are rather smooth in terms of water ice band depth variations (Filacchione et al., 2012; Hedman et al., 2013). This finding is a supplementary (but indirect) argument about the strong relationship between the surge amplitude and the regolith albedo, and will shed light on the nature of the interplay of the opposition effect mechanisms in the main rings. This will be detailed in Section 4.

The second minor trend that we observed from Fig. 3 is the repartition of the B ring in the (A, albedo) parameter space. In the macroscopic case (Fig. 3a), the morphological parameters seem to form a thick plateau as a function of ω_0 . In the microscopic case (Fig. 3b), a steep decrease is noted for the morphological parameters when $A_{1,13}$ increases. The thick plateau of A (or HWHM) with ω_0 reminds us of the invariance of the surge morphological parameters at high optical depth (τ) that we noted in Paper 1. Combining these two results suggests that the B ring morphological parameters of the surge are almost independent of the bulk albedo and the optical depth. This is consistent with the results of Déau and Helfenstein (2018), who obtained a strong linear correlation between ω_0 and τ in the B ring. Again, the implications of these results will be discussed in Section 4.

3.2. Variations of A and HWHM with VIMS spectral properties

In previous studies, the ring opposition effect morphology was found to depend strongly on wavelength, λ (Lumme and Irvine, 1976; Poulet et al., 2002; French et al., 2007; Salo and French, 2010; Déau et al., 2013a). In this paper, we use the results from the phase curves derived with ISS broadband images (using the CLEAR filters at $\lambda = 0.611 \pm 0.170 \mu\text{m}$ for the NAC and at $\lambda = 0.635 \pm 0.143 \mu\text{m}$ for the WAC, see Table 1 of Paper 1), meaning that wavelength effects are blurred with this dataset. Instead of studying the wavelength dependence of the morphological parameters, we propose a cross-correlation between the morphological parameters and the spectral properties of the rings. This cross-comparison is the first of its kind. Typically, the spectral properties are markers of water ice (the main component of the regolith layer on top of each macroscopic ring particle, Poulet and Cuzzi, 2002; Poulet et al., 2003), and the contaminants and their type of mixing (Cuzzi and Estrada, 1998; Poulet and Cuzzi, 2002; Ciarniello et al., 2011). Specifically:

- the water ice band depths (at $1.25 \mu\text{m}$, $1.5 \mu\text{m}$, and $2.0 \mu\text{m}$) are, inter alia, indicators of the purity of water ice in the ring regolith, see, e.g., Nicholson et al. (2008), Filacchione et al. (2012), Filacchione et al. (2013); Hedman et al. (2013). These studies found that the A and B rings have deeper water ice bands than the C ring and the Cassini Division.
- the spectral slope in the near infrared (NIR, $0.55 \mu\text{m} \leq \lambda \leq 0.95 \mu\text{m}$) is a marker of the broad-band absorber, see Cuzzi and Estrada (1998), Filacchione et al. (2012), Filacchione et al. (2013); Hedman et al. (2013), which could be nanophase iron (Clark et al., 2012). These studies showed that the concentration of the broad-band absorber is higher (meaning steeper slopes) in the C ring and the Cassini Division than it is in the A and B rings.
- the spectral slope in the near ultraviolet (NUV, $0.35 \mu\text{m} \leq \lambda \leq 0.55 \mu\text{m}$) is a marker of the ultraviolet absorber (Cuzzi and Estrada (1998); Poulet and Cuzzi (2002); Poulet et al. (2003); Hedman et al. (2013)). The distribution of the ultraviolet absorber is rather uniform across the main ring system, with a slight increase in the C ring and the Cassini Division (Hedman et al., 2013).

We have used the values of the $1.5 \mu\text{m}$ band depth (hereafter $\text{BD}_{1.5}$) derived by Hedman et al. (2013, Fig. 3) from the VIMS observation RDHRCOMPO01 of Rev 8. For the NIR and the NUV slopes (S_{NIR} and S_{NUV}), we also used the values derived by Hedman et al. (2013, Fig. 4) from the same VIMS observation. The radial profiles were retrieved using the digitization method from Déau et al. (2013b). The resulting cross comparison is presented in Fig. 4a–c for A as a function of $\text{BD}_{1.5}$, S_{NUV} and S_{NIR} , respectively. The vari-

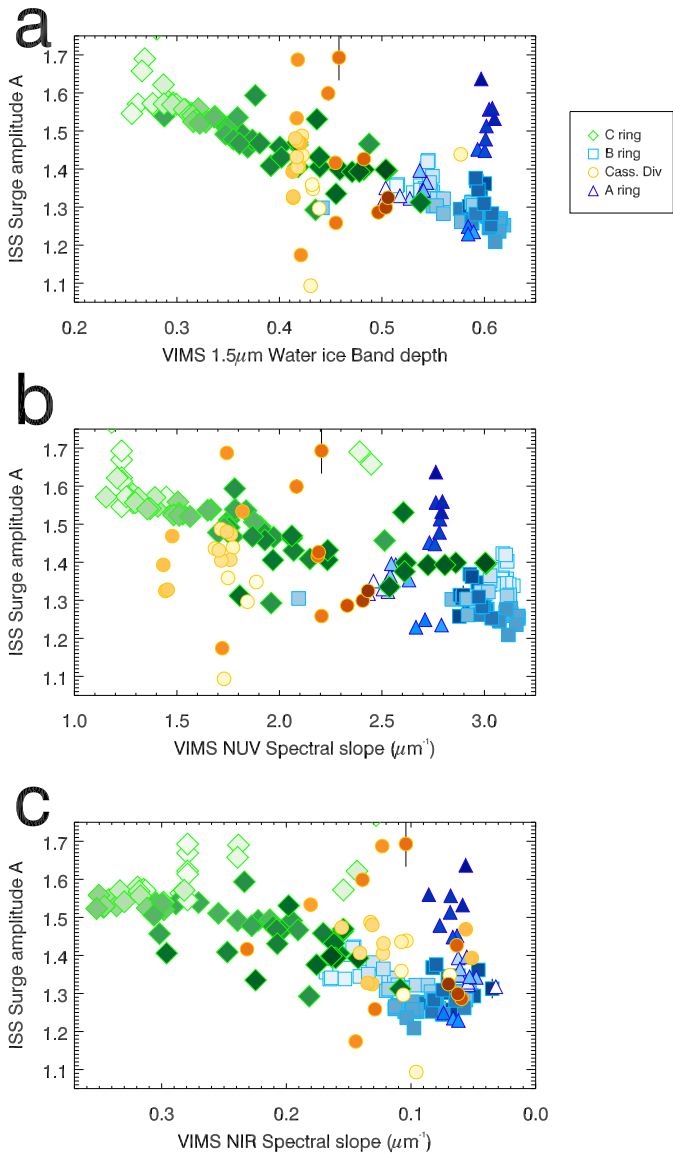


Fig. 4. Amplitude A of the ring opposition surge seen by ISS plotted as a function of the spectral properties of Hedman et al. (2013), using their VIMS observation RDHRCOMP001. Panel a: A is represented as a function of the 1.5 μm band depth $BD_{1.5}$. Panel b: the amplitude A is represented as a function of the near ultraviolet spectral slope S_{NUV} . Panel c: A is represented as a function of the near infrared spectral slope S_{NIR} (note that the x-axis is reversed to better compare panels a, b, and c). Symbol shapes correspond to different rings. Shading of color symbols (from lighter to darker) represents increasing distance to Saturn, see Fig. 2. (For interpretation of the references to color in this figure legend, the reader is referred to the web version of this article).

ations of HWHM are very similar, so we focus on the amplitude, but our findings work for both A and HWHM.

Our main trend of the cross comparison of A (or HWHM) and $BD_{1.5}$, S_{NUV} and S_{NIR} is the remarkably high strength of these correlations, compared to those found with the optical depth (see Fig. 6 of Paper 1). While the variations of A (or HWHM) seem saturated with τ , here the correlations of A (or HWHM) with $BD_{1.5}$, S_{NUV} and S_{NIR} clearly appear linear. This implies a very strong wavelength dependence of the morphological parameters of the surge, and confirms *de facto* the same origin for A and HWHM, and more particularly, an origin that excludes the role of τ (i.e. interparticle shadow hiding, see Déau 2015). We note that all the trends found in Fig. 4 (and Fig. A.1 for HWHM) are as strong as the one derived between the amplitude A and the regolith albedo

$A_{1.13}$, which is not surprising since $A_{1.13}$ is calculated from color ratios and band depths, see Hedman et al. (2013).

The second major trend that can be observed from Fig. 4 is that the correlations of A with the spectral properties are very similar. We observe a negative correlation for A and $BD_{1.5}$, as well as for A and S_{NUV} , while a positive correlation is noted between A and S_{NIR} (note that the x-axis is reversed in Fig. 4c). However, the distribution of the data points in the three parameter spaces is quite similar.

Our third major trend is that the correlation of A with $BD_{1.5}$ is stronger than the trends with spectral slopes and the regolith albedo. To quickly quantify the strength of these correlations, we use a simple linear fit on the previously cited quantities, and compare the values of their resulting correlation coefficient. For example, in the C ring, a linear fit of A - $BD_{1.5}$ leads to a correlation coefficient of -84.9% in Fig. 4a, whereas we found a correlation coefficient of -71.5% between A and $A_{1.13}$ in Fig. 3b. In the B ring, with the water ice band depth (Fig. 4a), the correlation of A with $BD_{1.5}$ is also strongly linear. This result is very specific to the water ice band depth, as the linear trends are less strong for the spectral slopes (Figs. 4b,c). Indeed, for this ring, a linear fit of A - $BD_{1.5}$ leads to a correlation coefficient of -71.6% in Fig. 4a against 8.5% for A - S_{NUV} (see Fig. 4b), and -46.3% for A - S_{NIR} (see Fig. 3b).

Another trend is the weaker correlations seen for the Cassini Division and the A ring, compared to the linear trends in the C ring and the B ring. The scatter in the Cassini Division appears larger for the spectral properties than it is as a function of optical depth (see Fig. 6 of Paper 1), which is puzzling. The scattering of Cassini Division points is more marked for $BD_{1.5}$ and S_{NUV} , while we distinguish for S_{NIR} a tendency of the Cassini Division points to join to the overall decrease of the outer C ring and B ring points. For the A ring, the variation of A (and HWHM) with the spectral properties is also scattered and undefined and does not seem to follow the same trend as the C ring and the B ring, but we should underline that we only have opposition data for the inner and middle parts of the A ring (see Paper 1).

Finally, in detail, there are slight disparities in the linear correlations observed in the parameter spaces (A , $BD_{1.5}$), (A , S_{NUV}), and (A , S_{NIR}). These variations can be grouped into two minor trends. The first one concerns the NUV spectral slope: in the C ring, basically S_{NUV} increases with increasing radial distance in Fig. 4b, however, when looking at the line formed by the C ring data points, we note a gap in the values of S_{NUV} between 2.2 and 2.5 μm^{-1} , which radially corresponds to the region located between the mid C ring and the outer C ring (i.e. the plateaus), as reported by Hedman et al. (2013). However, there is no similar gap with A , which suggests that the systematic differences of the ultraviolet absorber between the plateaus and other parts of the C ring are not relevant to the opposition effect. That trend is not observed for the water ice band depth (Fig. 4a). Interestingly, Hedman et al. (2013) noted that S_{NUV} is strongly correlated with the ice bands, and where they differ is mostly in the inner B/C rings. This result is illustrated in Fig. 4b with the outer C ring points not following a line with the inner B ring points, in contrast to Fig. 4a. The other minor trend is the behavior of the B ring for the spectral slopes: particularly in (A , S_{NUV}), the behavior of the B ring is isolated from the other rings, and forms a compact cloud of points (Fig. 4b). This indicates that the ultraviolet absorber should have a minor role in forming the B ring opposition effect, since it is weakly correlated with the surge morphology.

These cross-comparisons between the surge morphology and the spectral properties have allowed us to indirectly scrutinize the wavelength dependence of the opposition surge morphology, since $BD_{1.5}$, S_{NUV} and S_{NIR} belong to three distinct wavelength ranges. Because the spectral properties can be indirectly linked to the mechanisms of the opposition effect in terms of grain size and

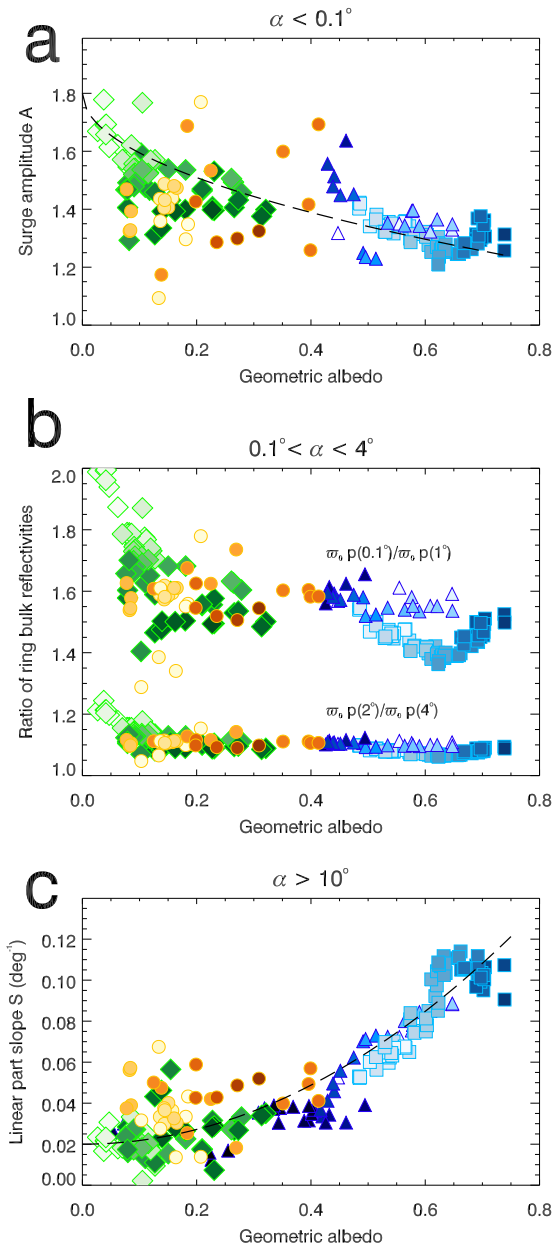


Fig. 5. Ratio of ring reflectivity at different phase angles versus albedo for the main rings. Panel a represents the ratio at $\alpha < 0.1^\circ$ (given by the amplitude A defined in Eq. (4)). Panel b represents the ratios $\bar{\omega}_0 p(0.1^\circ)/\bar{\omega}_0 p(1^\circ)$ on top and $\bar{\omega}_0 p(2^\circ)/\bar{\omega}_0 p(4^\circ)$ at the bottom. And panel c represents the behavior for $\alpha > 10^\circ$ (given by the slope S of the linear part defined in Eq. (6)). Shading of color symbols (from lighter to darker) represents increasing distance from Saturn, see Fig. 2. The dashed curves in Panels a and c are simple mathematical functions used to reproduce the global variation of each ensemble of data points. (For interpretation of the references to color in this figure legend, the reader is referred to the web version of this article).

mixing of contaminants (Poulet et al., 2002), it appears that the λ -dependence of the opposition effect varies from ring to ring. This result has major implications for the understanding of the predominance of the ring opposition effect mechanisms, and will be interpreted in Section 4.

3.3. Variations of the surge morphology with the phase angle range

We now present the trends of the surge amplitude and the slope of the linear part in Fig. 5 as a function of the geometric albedo A_v . The geometric albedo is just the I/F of each ISS phase curve at the smallest phase angle: $A_v = I/F(\alpha = 0^\circ)$, where

$I/F(\alpha = 0^\circ)$ is extrapolated from the data, as exact opposition is not reachable due to the finite size of the Sun, see Déau (2012).

We start with the slope (Fig. 5c). The trend of the slope is a monotonic increase with increasing geometric albedo. This trend is similar to that of the amplitude with the regolith albedo (Fig. 3b) in the sense that they're both monotonic, but the trend in Fig. 3b is a monotonic decrease. Interestingly, for the C ring and the B ring, the trend is stronger in the $(A, A_{1.13})$ parameter space than it is in the (A, A_v) parameter space, see Fig. 3b. In contrast, the A ring and the Cassini Division appear less scattered in the (A, A_v) parameter space. Finally, we note the net separation between the C ring and the B ring in the (A, A_v) parameter space, which was previously only visible in the (A, S_{NUV}) parameter space, see Fig. 4.

The amplitude of the surge is presented in Fig. 5a. As noted in Paper 1, the surge amplitude shows a different trend than the slope of the linear part of the phase curve (Fig. 5c). To specifically test the variation of the opposition effect mechanisms with phase angle, we use the methodology of Belskaya and Shevchenko (2000, their Fig. 6). According to this work, the relative contribution of each mechanism can be probed with the albedo dependence of the phase curve ratios at different phase angles. In detail, one must calculate the ratio of intensities at different phase angles, and display these intensities as a function of the albedo. To reproduce this method, we display the ratio of ring reflectivities $\bar{\omega}_0 p(0.1^\circ)/\bar{\omega}_0 p(1^\circ)$ and $\bar{\omega}_0 p(2^\circ)/\bar{\omega}_0 p(4^\circ)$ in Fig. 5b. We show these ratios between the amplitude of the surge (Fig. 5a) and the slope of the linear part (Fig. 5c) to display the increasing phase angle from the top of the figure to the bottom. In other words:

- Panel a of Fig. 5 represents the phase angle range $\alpha < 0.1^\circ$, by analyzing the surge amplitude. It is noteworthy to underline that our definition of the surge amplitude is really covering very small phase angles, contrary to other amplitudes that represent the ratio between 0.05° and 1° , see e.g. Buratti et al. (2009) or 0.3° and 5° , see Belskaya and Shevchenko (2000). Indeed, the surge amplitude from the linear model is the ratio between the maximum I/F at near 0° and an extrapolated point also near 0° corresponding to a hypothetical phase curve without any surge.
- Panel b represents the ranges $0.1^\circ < \alpha < 1^\circ$ and $2^\circ < \alpha < 4^\circ$. In this cases, we have used simple ratios between two phase angles, as in Belskaya and Shevchenko (2000).
- Panel c represents the range $\alpha > 10^\circ$, with the slope S of linear part defined for phase angles greater than 10° according to Eqs. (3) and (6).

Our results are the following: up to 4° (Fig. 5a and b), we note the same monotonic trend, while it starts to lose its strength with increasing phase angle. At phase angles larger than 4° , the ratio of ring reflectivities (defined by the slope of the linear part) increases with increasing geometric albedo. For asteroids, Belskaya and Shevchenko (2000, their Fig. 6) found the surge morphology trend with albedo to be non-monotonic, which is now confirmed in many other cases, see Déau et al. (2013b, 2018b). It is at $\alpha \approx 4^\circ$ that the albedo dependence (given by the derivative) changes its sign and then increases monotonically for larger α (Belskaya and Shevchenko, 2000, Fig.6). Our results are distinct from the findings of Belskaya and Shevchenko (2000), since the surge morphology-albedo trend remains monotonic for the rings, whatever the phase angle range. This difference could be due to: (1) the intrinsic nature of the surface (regolith of a solid body vs. regolith of small bodies layered in a ring) and (2) hypothetical mechanisms that might act at low albedo in the rings to compensate for the decrease observed for the asteroids.

3.4. Variations with radial distance to saturn

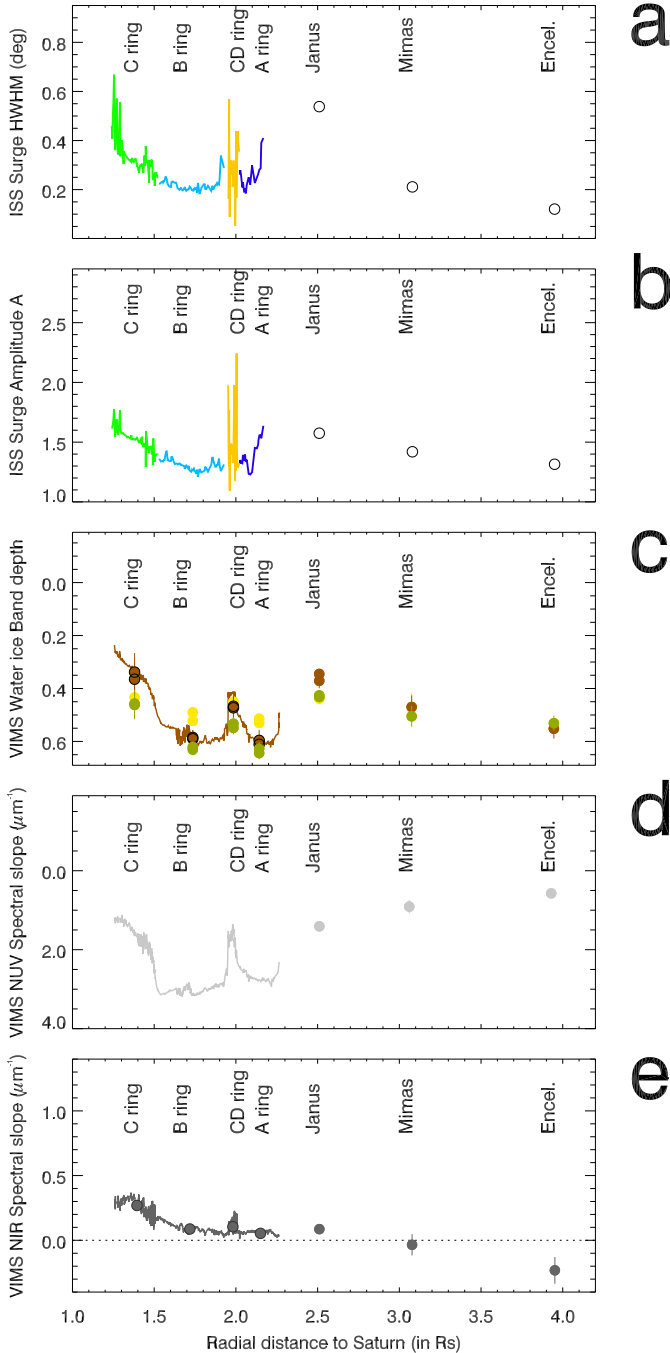


Fig. 6. Maps of the opposition effect surge morphology (Panels a and b) from the present study along with maps of the spectral properties (Panels c, d and e) of Saturn's main rings. Distances are in Saturn radii ($1 R_s = 60,330 \text{ km}$). Panels a and b: surge amplitude (A) and width of the opposition peak (HWHM) using the same color code as Fig. 5. Satellites values are from Verbiscer et al. (2007) in black circles. The Cassini dataset for the rings is obtained with the linear model on ISS data. Panel c: water ice band depths map from Filacchione et al. (2012) and Hedman et al. (2013) at $1.25 \mu\text{m}$ (green), $1.5 \mu\text{m}$ (brown) and $2.0 \mu\text{m}$ (yellow). Panel d: near ultraviolet (NUV) spectral slope S_{NUV} ($0.35\text{--}0.55 \mu\text{m}$) derived from the studies of Filacchione et al. (2012, 2013) and Hedman et al. (2013). Panel e: near infrared (NIR) spectral slope S_{NIR} ($0.55\text{--}0.95 \mu\text{m}$) derived from the studies of Filacchione et al. (2012, 2013) and Hedman et al. (2013). All spectral properties were observed at phase angles ranging from 10° to 40° , see Section 2.2 and Filacchione et al. (2012, 2013). Note that y-axis of panels c and d are reversed to better compare all the panels with each other. (For interpretation of the references to color in this figure legend, the reader is referred to the web version of this article).

We now want to compare the ring and satellite opposition effects in order to see how the opposition effect varies beyond the main ring system. This comparison was made by Déau et al. (2009); however, that study did not include small satellites near the A ring, like Janus, which we include here. In Déau et al. (2018b), a similar map was also presented, from the C ring to the distant irregular satellite Ymir; however, the data for the main rings were averaged. In the present study, we have followed the methodology of Déau et al. (2009, 2018b) and Filacchione et al. (2013), but we have improved it by showing the radial variations within the main ring system. For the main rings' morphological parameters, we continue using the values from Paper 1 and depicted in Fig. 2, while for the satellites (up to Enceladus), we have used the parameters of Verbiscer et al. (2007, their Fig. S1). Note that we exclude the E ring here, as we have not yet processed the ISS images containing the opposition surge of this ring. However, this ring was studied along with nearby satellites in Verbiscer et al. (2007) and Déau et al. (2009) using Earth-based and ground-based observations. Note that the D ring has also been removed. Indeed, while its surge morphology is well known (see Paper 1), its spectral properties are less well constrained, see Hedman et al. (2007).

Note that Verbiscer et al. (2007)'s amplitude was not defined the same way than in our study: in their case the amplitude is $I_{\text{peak}}/I_{\text{bkgd}}$, the exponential opposition surge I_{peak} relative to the mean intensity I_{bkgd} . Due to the intrinsic nature of the surge, I_{bkgd} is always less than I_{peak} , meaning that their amplitude is always less than unity. By contrast, in our case, the amplitude is defined as the ratio of the surge intensity over the total in such way that $(I_{\text{peak}} + I_{\text{bkgd}})/I_{\text{bkgd}}$, following the original formulation of Mishchenko and Dlugach (1992, their Eq.(5)). As a result, by comparing the two formulas, there is a discrepancy of 1 between the amplitude of Verbiscer et al. (2007) and the present values. The amplitude is thus just shifted by +1 for the satellite amplitude values.

We present our main results as a map displaying the morphological parameters as a function of the distance to Saturn from the C ring to Enceladus. Because maps also exist for the spectral properties studied here ($BD_{1.25}$, $BD_{1.5}$, $BD_{2.0}$, S_{NUV} and S_{NIR}), see Filacchione et al. (2012, 2013), we decided to compare them with our own maps.

Fig. 6 displays the maps of the opposition surge morphology (Panels a and b), as well as maps of the band depth (in Panel c) and spectral slopes S_{NUV} and S_{NIR} (Panels d and e). From the C ring to Enceladus, the variations of the opposition surge morphology are strongly correlated with $BD_{1.25}$, $BD_{1.5}$, and $BD_{2.0}$. With a few exceptions that we will detail further, the agreement between these maps is very satisfactory. The common trend found can be summarized in this way: up to Enceladus, which orbits at 4 Saturn radii, a double bowl-shaped distribution is observed with extrema on the B ring and on Enceladus.

The exceptions are the following:

- For the rings, the surge morphological parameters and the spectral parameters all appear to be smallest in the B ring; note, however, that the y-axis is reversed in the case of the water ice band depths (Fig. 6c) and the NUV spectral slope (Fig. 6d), meaning that the surge morphology is actually anti-correlated with these properties. In fact, the surge morphology is only positively correlated with the NIR spectral slope (Fig. 6e).
- When grouping the satellites Janus, Mimas and Enceladus, we note an overall decrease of the surge morphology and the spectral properties with Saturn's distance, except for the water ice

band depths of the satellites for which we note an increase with radial distance to Saturn (Fig. 6c).

- The NUV spectral slope appears to be the only parameter that has a distinct behavior for the rings and the satellites compared to the other parameters (Fig. 6d). Indeed, for all the other parameters, the B ring and Enceladus appear to have extreme values: for the surge morphology, it means the smallest amplitude and angular width (Fig. 6a,b); for the water ice band depths, it means the strongest bands (Fig. 6c); for S_{NIR} , it means small to negative values (Fig. 6e). However, for S_{NUV} , see Fig. 6d, while the B ring has the highest value of S_{NUV} , Enceladus, at the opposite, has the smallest value. Interestingly, S_{NUV} was the parameter with the largest scatter in the (surge morphology, spectral property) parameter space, see Fig. 4. It means that while there is indeed a correlation between the surge morphology and the NUV spectral slope, there are other factors that might intervene in one and not necessarily the other.

These results will be discussed in the framework of the coherent backscattering induced by regolith properties in the next section.

4. Discussion

4.1. Implications from the phase dependence of the spectral properties

In the present work, we have compared the opposition surge morphology to several spectral properties that were taken between 12° and 41° of phase angle. However, spectral properties also show phase angle variations, thus we propose to review them here.

In Hedman et al. (2013), VIMS spectral properties were assumed to have little dependence on the viewing geometry (α and B , the spacecraft elevation that controls if the rings are seen on the lit side or the dark side). However, Filacchione et al. (2014) showed that there is a strong phase dependence of the VIMS spectral properties. We summarize the interpretations of these two studies as follows:

- A first way to explain the phase dependence of the spectral properties is to consider that the spectral properties do not represent variations in the ring phase function, but instead mostly indicate changes in the ring particles' wavelength-dependent albedos, see Hedman et al. (2013). This is why Hedman et al. (2013) claimed low-phase data such as VIMS_008RI_RDHRCOMP001 were enough to infer micro-properties like regolith structure and composition. This claim was based on the “observed” lack of multiply-scattered light in water ice band depths at high phase angle. In detail, the model of Hedman et al. (2013) is based on ring particles that are highly backscattering. By observing the light reflected by the rings at high phase angle or from the unlit side, they inferred that multiple scattering between ring particles should be a larger fraction of total light received by the detector. In this case, multiple scattering should induce deeper water ice bands than single scattering should. However, they noticed small differences between lit low phase, lit high phase and unlit low phase water ice band depths (see Hedman et al. (2013, Fig. 3)), which they interpreted as a proof that only a small fraction of the light was multiply scattered. They attributed the lack of multiple scattering to the flatness of the layer of ring particles, which de facto reduces multiple scattering.
- A second way to explain α -dependence of the spectral properties is to consider that these properties do represent variations in the ring phase function, see Filacchione et al. (2014). However, instead of assuming one size for the ring particles, Filacchione et al. (2014) conjectured that different functions

could be used to model the angular response of the light scattered by the ring: large particles (with size $\gg \lambda$) have a backscattering response, while small grains are more forward scattering and isotropic. In detail, Filacchione et al. (2014) derived the phase angle variations of the spectral slopes and the water ice band depths with a better phase angle resolution than Hedman et al. (2013). Some of their results for the NUV spectral slope are reported in Fig. 7. Their model complements the one of Hedman et al. (2013) by adding the size distribution dimension in the ring phase function.

We now revisit the work of Hedman et al. (2013) and Filacchione et al. (2014) in the light of our new results about the correlation between the surge morphology and the spectral properties:

- Another way to explain the phase dependence of the spectral properties is to consider that the spectral properties do not represent variations in the ring particle phase function, but the regolith grain phase function. While envisaged by Hedman et al. (2013), this theory was tested in the work of Poulet et al. (2002). We now test this hypothesis by retrieving the color ratios $CR_{\text{GRN-UV}}$ of Déau and Dones (2018) for the main rings over a large range of phase angles (see Fig. 7). Indeed, because Poulet et al. (2002) and Cuzzi et al. (2002) use HST data, they only cover phase angles $\alpha \leq 6^\circ$. To model this color ratio, we use the coherent backscattering model of Poulet et al. (2002), based on the Shkuratov et al. (1999b) theory:

$$CR_{\text{GRN-UV}} \sim \frac{2 + \left[\sqrt{1 + (4\pi L_{\text{GRN}} \sin(\alpha/2)/\lambda_{\text{GRN}})^2} \right]^{-1}}{2 + \left[\sqrt{1 + (4\pi L_{\text{UV}} \sin(\alpha/2)/\lambda_{\text{UV}})^2} \right]^{-1}} \times \exp[(k_{\text{UV}} - k_{\text{GRN}})\alpha], \quad (13)$$

where L_i and k_i are the parameters of the Shkuratov et al. (1999b) model for the wavelength λ_i . The values of L_i and k_i for the green and ultraviolet filters are retrieved from Poulet et al. (2002, Table VI). In the Shkuratov et al. (1999b) model, only multiple scattering is assumed, which allows us to constrain the theories of Hedman et al. (2013) and Filacchione et al. (2014). Indeed, in Fig. 7, we demonstrate that the claim of Hedman et al. (2013) about the lack of multiple scattering at high phase angle is correct for the color ratio as well. Indeed, the best fits at low phase angle with HST data do not fit the ISS data at high phase (see right panels of Fig. 7). However, contrary to the claim of Filacchione et al. (2014), it is the combination of various values of roughness and scattering length (not the grain size) that can reproduce the behavior of the color ratio at low phase and at high phase. Thus, we have demonstrated that regolith multiple scattering can reproduce the ring scattering behavior at low phase, just as the ring particle single scattering does (Dones et al., 1993).

4.2. The roles of regolith composition, grain size, porosity, and roughness in the ring opposition effect

In the previous section, the strength of the correlations between the surge morphology and the spectral properties suggested that both the surge morphology and the radial variations of spectral properties were caused by a common mechanism, which could be coherent backscattering. Indeed, coherent backscattering can affect the water ice band depths at the moderate phase angles (12 – 41° , see Section 2.2) seen with VIMS by Hedman et al. (2013), because Kolokolova et al. (2010) showed it successfully reproduced phase angle variations from 0.05° to 19° of water ice band depths of

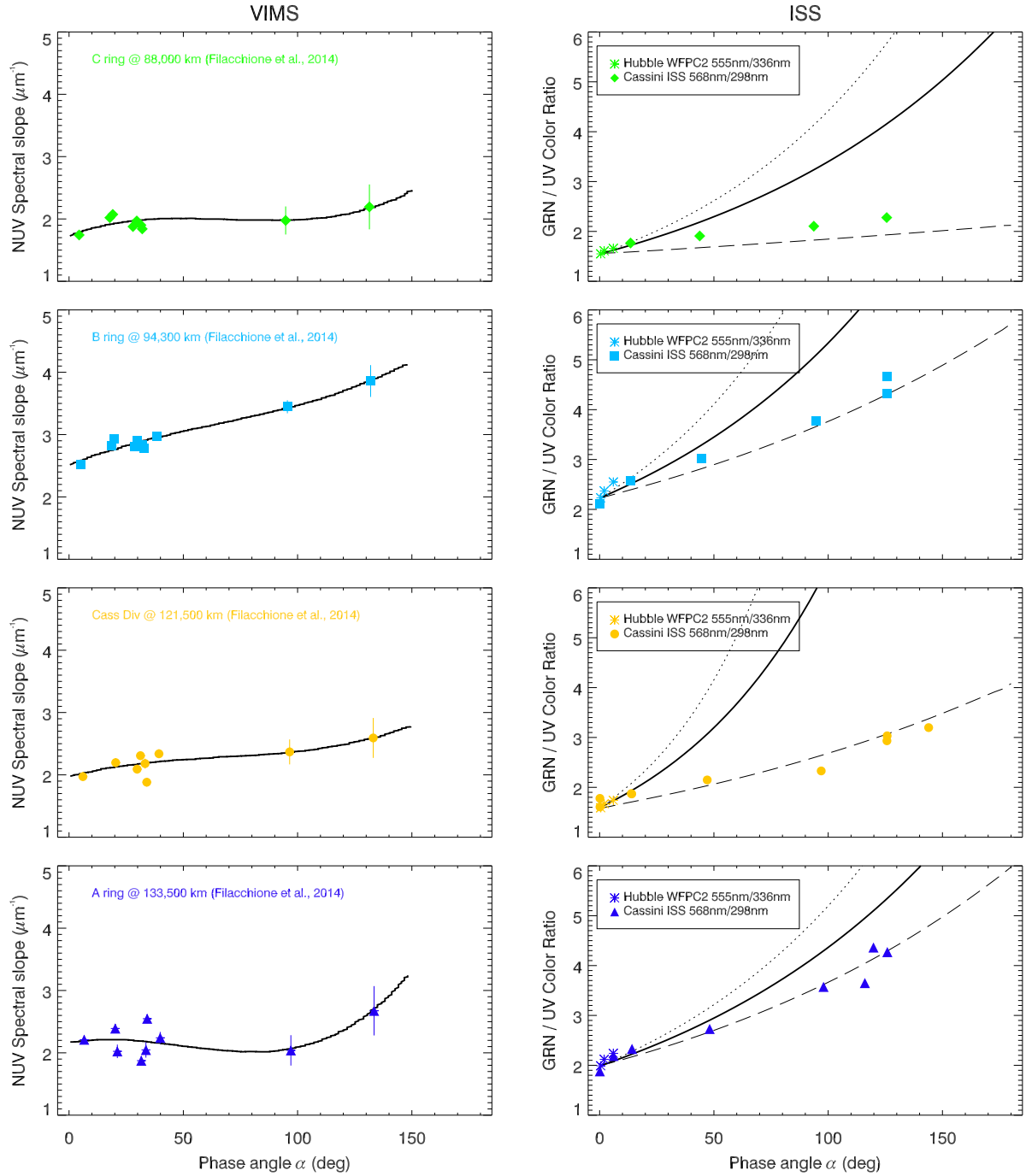


Fig. 7. Left: NUV spectral slopes for specific regions in the main rings from VIMS data (Filacchione et al., 2014, Fig. 14) and Right: GRN / UV color ratios for the same regions using ISS data (Déau and Dones, 2018). The HST/WFPC2 color ratios of Cuzzi et al. (2002) are added as a reference. On the left, the solid curve is a simple morphological model to fit the data. On the right, the solid curve is the color ratio of Eq. (13) using the parameters k and L of the best fit to the phase curves of Poulet et al. (2002, Table VI). Dashed and dotted curves correspond to the color ratios using, respectively, the minimum and maximum values for the parameters k and L of Poulet et al. (2002, Fig. 14). (For interpretation of the references to color in this figure legend, the reader is referred to the web version of this article).

icy satellite regoliths also seen by VIMS. Here, we further investigate the predictions of a coherent backscattering model by comparing the expected behaviors of this mechanism with the surge morphology. We use the model of Mishchenko (1992), which calculates directly the half width at half maximum (HWHM_{cb}) for an ensemble of polydisperse, homogeneous and spherical scatterers (called “grains”) with the Lorenz-Mie theory that includes coherent backscattering, since this mechanism is embedded within Maxwell’s equations. The code is in Fortran, and calculates the

coherent backscattering angular width as:

$$\text{HWHM}_{cb} = \frac{\varepsilon \lambda}{2\pi} C_{sca} (1 - \langle \cos \Theta \rangle) \frac{3(1-P)}{4\pi r_0^3}, \quad (14)$$

where ε is a constant, λ is the wavelength, C_{sca} is the scattering cross section, $\langle \cos \Theta \rangle$ is the mean cosine of the scattering angle, P is the medium porosity, and r_0 is the effective grain radius defined in the gamma size distribution:

$$n(r) \propto r^{(1-3b)/b} \exp\left[-\frac{r}{r_0 b}\right], \quad (15)$$

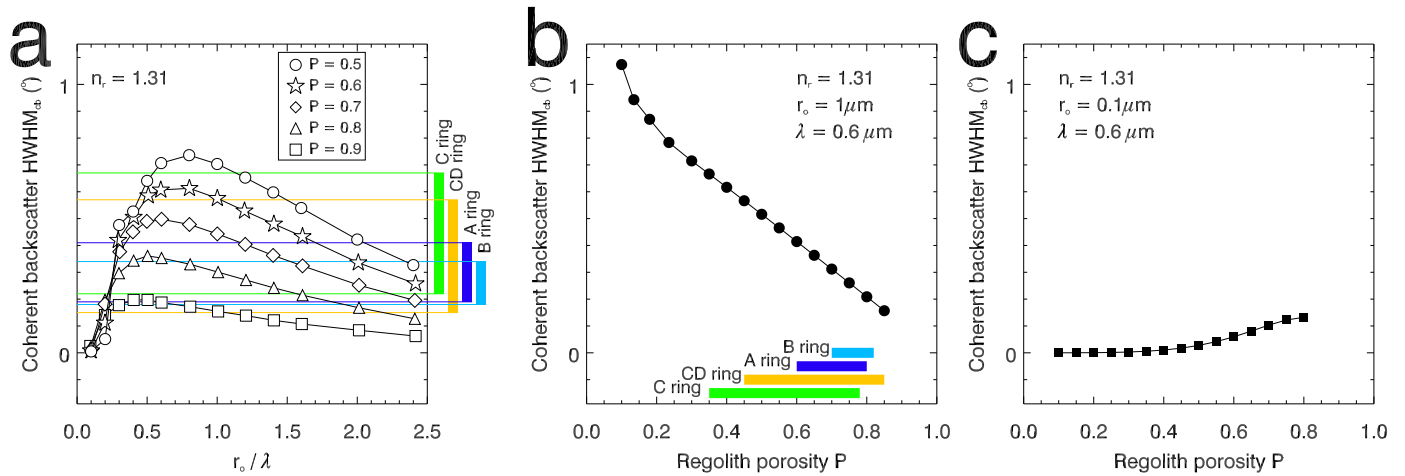


Fig. 8. Numerical simulations of the coherent backscattering using Eqs. (14) and (15) with the real refractive index set to 1.31 to be consistent with Mishchenko (1992, Fig.1). – Panel a: HWHM_{cb} as a function of the dimensionless ratio between the mean grain size r_0 and the wavelength λ to reproduce the result of Mishchenko (1992, Fig.1). Comparatively to Mishchenko (1992), additional values for $P = 0.5$ are added. On the right of the graph, the range of values of the ISS angular width HWHM is plotted, and the extrema values are indicated by horizontal lines within the graph. – Panel b: HWHM_{cb} as a function of the regolith porosity P for a set of input parameters that include $r_0 = 1 \mu\text{m}$ and $\lambda = 0.6 \mu\text{m}$ in order to test the case where $r_0 > \lambda$. The range of porosity values for each ring is depicted with the horizontal bars and is obtained from the match of the coherent backscattering angular width HWHM_{cb} from Eq. (14) and the ISS surge HWHM. – Panel c: HWHM_{cb} as a function of the regolith porosity P with $r_0 = 1 \mu\text{m}$ and $\lambda = 0.6 \mu\text{m}$ to test the case $r_0 < \lambda/2$.

which we take to have a narrow width of $b = 0.04$ as in Mishchenko (1992). Note that in the rings' case, this model assumes that the scatterers are whole regolith grains constituting the outer regolith layer covering centimeter- to meter-sizes ring particles rather than wavelength-scale structural defects covering and/or within regolith grains and that the regolith porosity is representative of the separation between these grains. It also assumes that small grains do not clump into regolith aggregates.

As this coherent backscattering model depends on the composition, the grain size, and the regolith porosity, we propose a review of the coherent backscattering predictions with the current values of these parameters, if known.

4.2.1. Regolith porosity

With Eq. (14), variations of the width of the coherent backscattering peak can be significant when the structure of the medium is changed. For example, if the composition is kept constant (with a real refractive index set to 1.31), HWHM_{cb} is a decreasing function of the porosity for most of the values of the dimensionless ratio between the grain size r_0 and the wavelength λ , see Mishchenko (1992, Fig.1) and Fig. 8a. We have also calculated HWHM_{cb} as a function of the porosity of the medium for two cases: one when the grain size is larger than the wavelength ($r_0 = 1 \mu\text{m}$ and $\lambda = 0.6 \mu\text{m}$), see Fig. 8b; the other being for $r_0 < \lambda/2$ (i.e. $r_0 = 0.1 \mu\text{m}$ and $\lambda = 0.6 \mu\text{m}$), see Fig. 8c. With the latter case ($r_0 < \lambda/2$), the trend is a slight increase of HWHM_{cb} with increasing porosity. However, no porosity value leads to a match between the ISS HWHM values and the HWHM_{cb} values, as the HWHM_{cb} values are very small ($\text{HWHM}_{cb} \leq 0.13^\circ$), see Fig. 8c. This constraint on the grain size will be further analyzed in the discussion. With the former case ($r_0 > \lambda$), the values of HWHM_{cb} can easily match the ISS HWHM values for various ranges of regolith porosity, see Fig. 8b. These ranges are reported in Table 1.

Note that these cases only apply to water ice-based compounds, as the real refractive index is set to 1.31 (as in the study of Mishchenko 1992), which is close to pure water ice's n_r (indeed $n_r = 1.33$ at $\lambda = 0.6 \mu\text{m}$, see Warren 1984 and Warren and Brandt 2008).

As a result, to reproduce the observed trend of the ISS HWHMs with the regolith porosity, the A and B ring particles must have regolith surfaces that are more porous than those in the C ring and

Table 1

Derivation of the acceptable range of porosity values from the match of the coherent backscattering angular width HWHM_{cb} from Eq. (14) and the ISS surge HWHM. The other input parameters of the simulations are: $r_0 = 1 \mu\text{m}$, $\lambda = 0.6 \mu\text{m}$, and $n_r = 1.31$, see Fig. 8b.

Ring	Porosity range	Average Porosity P_{mean}
A ring	$0.60 \leq P \leq 0.80$	0.70
B ring	$0.70 \leq P \leq 0.82$	0.76
Cassini Division	$0.42 \leq P \leq 0.85$	0.63
C ring	$0.35 \leq P \leq 0.78$	0.57

the Cassini Division, see Fig. 8b. This is also what was qualitatively derived in Fig. 14b of Paper 2. However, when this filling factor was converted to an actual regolith depth, it led to inconclusive results (note also that the porosity values found in Paper 2 are very large: $P \geq 0.9$, but they assumed a pure intra-particle shadow hiding contribution, whereas here, we assume a pure coherent backscattering contribution). Paper 2 concluded that these inconclusive results did not necessarily mean that the regolith porosity cannot be a serious candidate to explain the surge morphology and the spectral properties, but instead that very little is known about the regolith porosity, and without additional constraints, it was difficult to predict accurate variations of this parameter across the main rings.

As a matter of fact, additional constraints that have not been considered in Paper 2 can be used here to validate or invalidate the conjecture that the A and B ring particles have regolith surfaces that are more porous than those in the C ring and the Cassini Division. Constraints on the porosity of the regolith on top of the ring particles are in fact related to the dynamical activity of these particles⁴ via the restitution coefficient ϵ_r . This parameter is a measure of the energy loss after one encounter between two ring particles ($\epsilon_r \rightarrow 0$ when all kinetic energy was lost in deforming the impactors, and $\epsilon_r \rightarrow 1$ when the collision is elastic). We propose to look at the porosity-dependence of ϵ_r from

⁴ We must emphasize that the regolith porosity P is “a priori” totally independent on the porosity of the ring layer P_{ring} , which is described by many studies as the ring filling factor $D \equiv 1 - P_{\text{ring}}$, see (Salo and Karjalainen, 2003). The fact that $P \neq P_{\text{ring}}$ is simply demonstrated here because we obtain higher values of regolith porosity in the rings that are known to be more compact.

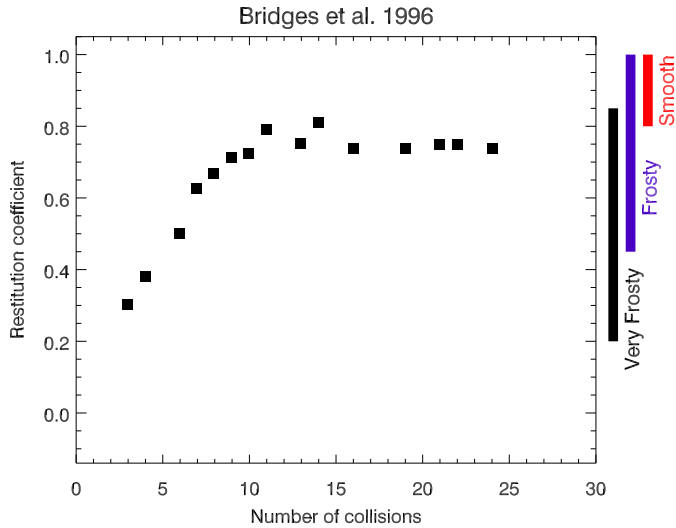


Fig. 9. Variation of the restitution coefficient ϵ_r from the study of Bridges et al. (1996) that are used in the present section as a porosity dependence of the restitution coefficient. ϵ_r as a function of the number of consecutive collisions between an ice sphere and flat ice surface, both coated with a layer of water ice frost at a constant impact velocity of $0.5 \text{ cm}\cdot\text{s}^{-1}$, see Bridges et al. (1996). On the right, the ranges of ϵ_r values for “smooth”, “frosty”, and “very frosty” textures are impact velocity-dependent laws for ϵ_r and are respectively from Hatzes et al. (1988, Figs. 11 and 14), and Bridges et al. (1984, Fig. 1). Note that impact velocities in the three cited cases are $< 2 \text{ cm}\cdot\text{s}^{-1}$.

previous studies, which could allow us to narrow down the validity domain of the regolith porosity knowing the acceptable range of values for ϵ_r . Because this is a novel approach, we propose to go deeper in the explanation of the different factors that affect ϵ_r . It is well known that ϵ_r depends on the impact velocity (which is about a few $\text{mm}\cdot\text{s}^{-1}$, see Schmidt et al. 2009), and several empirical “laws” of ϵ_r as a function of the impact velocity have been derived from laboratory experiments of bouncing ice particles (Bridges et al., 1984; 1996; Hatzes et al., 1988). Interestingly, these “laws” depend on the surface state of the ice particles, fixed arbitrarily to be “very frosty”, “frosty” or “smooth”, and referring to the roughness of the ice particles. However, the recent study of Shimaki and Arakawa (2012) shows that the regolith porosity plays a large role in the result of a collision. These results are in agreement with the experiments of Bridges et al. (1996), who showed that ϵ_r would increase with the number of collisions (see Fig. 9a) at a constant impact velocity of $0.5 \text{ cm}\cdot\text{s}^{-1}$, even though the work of Shimaki and Arakawa (2012) refers to impact velocities orders of magnitude larger than those likely to be relevant to rings. Bridges et al. (1996) indicated that the values of ϵ_r are very low for the first collisions when the frost layer is loose, but they steadily increase and reach an equilibrium value of $\epsilon_r \approx 0.8$ when the frost layer becomes compacted. Consequently, the underlying result of Bridges et al. (1996) is that the restitution coefficient is an increasing function of the filling factor (and a decreasing function of the regolith porosity).

These results allow the roughness terms “very frosty”, “frosty” or “smooth” to be reinterpreted in terms of porosity. The elasticity “laws” of Bridges et al. (1984, 1996) and Hatzes et al. (1988) provide different ranges for the value of ϵ_r , for example, the “very frosty” law of Bridges et al. (1984, Fig. 1) and the “frosty” law of Hatzes et al. (1988, Fig. 14) are related to moderate to very high restitution coefficient values ($0.2 \leq \epsilon_r \leq 1$), and may correspond to high porosities, while the “smooth” law of Hatzes et al. (1988, Fig. 11) related to only very high restitution coefficient values ($\epsilon_r > 0.8$), may correspond to low porosities. This qualitative conversion indicates that the C ring and the Cassini Division should

be close to a “frosty” state, whereas the A and B ring might be even “frostier”.

To complete our approach, the values of ϵ_r are estimated in terms of optical depth dependence. It is well-known that high- τ regions have more collisions per orbit than low- τ regions because the collision frequency ν_c is given by:

$$\nu_c \propto \Omega \tau, \quad (16)$$

for small τ . Here Ω is the keplerian frequency $\Omega = \sqrt{GM_h/R^3}$, G is the gravitational constant, M_h is Saturn’s mass and R is the distance to Saturn (Brahic, 1977; Schmidt et al., 2009). (If the self-gravity of the rings is important, the collision rate can be orders of magnitude higher, e.g., Wisdom and Tremaine (1988).) Therefore, high- τ regions should have significantly higher values of ϵ_r than low- τ regions. However, ϵ_r should not linearly increase with τ and might reach an equilibrium. Indeed, a “moderately smooth” law from Hatzes et al. (1988) was used by Schmidt et al. (2009) to simulate the formation of self-gravity wakes. Their study shows that “moderately smooth” particles prevent the formation of self-gravity wakes (Schmidt et al., 2009, their Fig. 14.6). This result means that we can eliminate the range $\epsilon_r > 0.8$ (i.e., low porosities) for the A and B rings, in agreement with the range of values derived in Fig. 8b from our coherent backscattering simulations (i.e. $0.70 \leq P \leq 0.82$ for the B ring and $0.60 \leq P \leq 0.80$ for the A ring).

However, the present approach is very simplistic. Indeed, even though the average elasticity is likely to adjust dynamically to a larger value for larger optical depth, as implied by Eq. (16), the average elasticity should follow the energy balance between viscous stirring and dissipation (see Goldreich and Tremaine 1978; impact velocities adjust to give the correct rate of dissipation), rather than because higher impact frequency is affecting the surface properties of the ring particles.

All in all, the comparison of Figs. 8b and 9 b leads to the idea that the A and B rings should have ring particles with a high regolith porosity (that might correspond to a “very frosty” state), while the C ring and the Cassini Division should have less porous regoliths that correspond to a “frosty” state. It would be interesting to see the impact of using different ϵ_r -laws with N-body simulations coupled to ray-tracing model on phase curves, since so far, simulations coupled to ray-tracing model used the same ϵ_r -laws regardless the ring.

4.2.2. Composition

Pure water ice is characterized by a spectral behavior that results in: (1) a slightly positive NUV spectral slope ($0.35\text{--}0.55 \mu\text{m}$) and (2) a small negative NIR spectral slope ($0.55\text{--}0.95 \mu\text{m}$) (Warren et al., 2006), with some variations caused by different effective size, porosity and roughness of the regolith (Dadic et al., 2013). The smaller opposition surge of the B ring, compared with the C ring and the Cassini Division (Fig. 2), can be explained with the ring composition using coherent backscattering theory because the B ring is believed to have purer water ice than the other rings, as is well known (e.g., Filacchione et al. (2014)). Indeed, theoretically, pristine water ice leads to narrower coherent backscattering peaks than other materials. This has been demonstrated with the coherent backscattering model by Mishchenko (1992), who showed that by varying only the composition, the angular width of the coherent backscattering peak (HWHM_{cb}) was smaller for pure water ice (see Fig. 1 of Mishchenko 1992) than for materials with higher real refractive index values (see Fig. 3 of Mishchenko 1992). Also, the hypothesis that the B ring has purer water ice than the other rings is validated by other datasets, including the B ring’s water ice band depths (Nicholson et al., 2008; Filacchione et al., 2012; 2013; Hedman et al., 2013) and the B ring’s high geometric albedo (Fig. 5). Even though, in practice, our assumptions about the composition lead to the observed behavior of the ring opposition effect,

to improve the fidelity of the model, the values of the real refractive index of the materials that comprise the rings are necessary. Water ice has a real refractive index of $n_r = 1.33$ and an imaginary refractive index of $n_i = 4.4 \times 10^{-9}$ at $\lambda = 0.6 \mu\text{m}$ (Warren, 1984; Warren and Brandt, 2008). According to Poulet et al. (2003) and Ciarniello (2012), contaminants in the rings can be either:

- amorphous carbon (with $n_r = 2.00 \pm 0.10$ and $n_i = 0.50 \pm 0.30$ at $\lambda = 0.6 \mu\text{m}$, see Rouleau and Martin 1991; Zubko et al. 1996),
- Titan tholins (with $n_r = 1.60 \pm 0.10$ and $n_i = 0.060 \pm 0.005$ at $\lambda = 0.6 \mu\text{m}$, see Khare et al. 1984; 1993; 1994),
- Triton tholins (with $n_r = 1.65 \pm 0.05$ and $n_i = 0.0030 \pm 0.0002$ at $\lambda = 0.6 \mu\text{m}$, see McDonald et al. 1994; Ciarniello 2012), or
- silicates (with $n_r = 1.70 \pm 0.05$ and $n_i = 0.00010 \pm 0.00005$ at $\lambda = 0.6 \mu\text{m}$, see Pollack et al. 1994; Fearnside et al. 2016).

A final compound to consider is nanophase iron. According to Pieters et al. (2000) and Noble et al. (2007), nanophase iron (npFe⁰) produces a strong positive spectral slope across the visible to near-infrared spectra (i.e., the so-called “spectral reddening”, which is well-known in Saturn’s ring spectroscopic investigations, see e.g. Cuzzi et al. 2009):

- nanophase iron should have the same real refractive index as iron ($n_r = 2.87 \pm 0.10$ and $n_i = 3.35 \pm 0.5$ at $\lambda = 0.67 \mu\text{m}$ according to Ordal et al. 1988), however, this material has not been used yet in near ultraviolet to near infrared spectral modeling.

Note that in Eq. (14), the influence of the composition on the opposition peak width is considered only with regard to the real part of the refractive index, and the imaginary part is ignored, meaning that absorption within the grains is ignored. The value of n_i can affect the results only through absorption, i.e., the intensity decreases as $\exp(-4\pi \ell n_i / \lambda)$, where ℓ is the characteristic distance that the light at a wavelength λ goes through the grain. Indeed, for the quantities in Eq. (14) – the scattering cross-section and the phase-function asymmetry parameter – the effect of strong absorption may be noticeable (e.g., Hansen and Travis, 1974). For most of the compounds believed to be present in the rings – water ice, tholins, and silicates – the value of n_i is quite small at visual wavelengths, and neglecting absorption is justified. On the other hand, for materials such as iron and amorphous carbon, with large n_i values (see above), absorption could be significant. However, the major issue to overcome with these compounds is the lack of absorption band detections. For example, amorphous carbon has several bands at 3.38, 3.41, and 3.48 μm , and silicates at 9.7 and 18 μm , none of which have been detected so far (Lynch et al., 2000; Brown et al., 2006; Nicholson et al., 2008). As a result, it is justified to neglect absorption at first order for these compounds, even though we consider scattering.

Mishchenko (1992, Figs. 1, 2, 3) provided simulations of the angular width HWHM_{cb} for a subset of values of composition (via the real refractive index n_r), grain size and regolith porosity. In Fig. 10, we have extended the values of n_r used by Mishchenko (1992) to cover higher values for amorphous carbon and nanophase iron, and we have calculated HWHM_{cb} for different porosities (with an additional value at $P = 0.5$ that is close to the values for the C ring and the Cassini Division seen in Fig. 8b and Table 1).

In Fig. 10, we have superimposed the observed surge width from the ISS data to our simulations. It can be seen that only water ice-based compounds ($n_r = 1.31$) offer a good match between the ISS HWHM values and the HWHM_{cb} values. However, with this value of n_r , most sizes and most porosities can fit the ISS data. When increasing the real refractive index, with $n_r = 1.60$ and $n_r = 1.70$, which is close to the values for Titan tholins, Triton tholins, and silicates, most of the HWHM_{cb} values where the ratio

$r_0/\lambda \sim 0.5$ are larger than the ISS width values. We conclude that if the coherent backscattering is driven by small grains of the size of $\lambda/2$, these grains must be pure water ice and embedded in a porous regolith layer ($P > 0.5$).

To constrain the composition more accurately (by separating the water ice from the contaminants), we need to consider how the water ice is mixed with the contaminants. Indeed, spectral modeling has shown that the types of mixture are much more model-dependent than the grain size, meaning that it is almost always possible to find a grain size value to reasonably fit the data, whereas the type of mixture can prevent a fit from converging, see, e.g., Poulet et al. (2003). Types of mixtures include: areal, intimate, and intra, see, e.g., Poulet et al. (2003) and Ciarniello (2012). We also examine the case of the “coat” mixture. A diagram of these mixtures is represented in Fig. 11. These types of mixtures are now reviewed in light of the present results. However, we must underline that the coherent backscattering code used here assumes a homogeneous medium, which seems incompatible with the concept of a mixture. A way to overcome this issue is to use effective compositions. Indeed, considering the randomness of multiple scattering in the coherent backscattering, it seems acceptable to use effective compositions when calculating the refractive index of mixtures.

- *Areal mixture.* An areal mixture consists of isolated contaminant grains on the surface (see Fig. 11). In this type of mixture, the light interacts either with ice grains or with contaminant grains, but not both. This type of mixture has not been modeled for the rings yet (Cuzzi et al., 2009). To test this hypothesis, we again use the coherent backscattering predictions seen in Fig. 10 to seek clues to the ring composition. As seen in Fig. 10, coherent backscattering simulations show that materials with higher real refractive indices ($n_r = 2.90$) have larger HWHM_{cb} than materials with lower real refractive indices ($n_r = 1.31$). Previous composition calculations by Poulet et al. (2003) have indicated that fitting the C ring spectra does not require free amorphous carbon contrary to the A and B rings spectra, meaning the C ring might contain less amorphous carbon (i.e. less dark contaminants) than the A and B rings. For the sake of the calculations, we assume: (1) the areal mixture consists of small grains of contaminants ($r_0/\lambda \leq 0.2$ and $n_r \geq 1.6$) producing the dominant part of the backscattering; (2) the contaminants are more abundant in the A and B rings than in the C ring, as claimed by Poulet et al. (2003). If we consider the coherent backscattering predictions seen in Fig. 10, the areal mixture hypothesis could be valid for contaminants such as tholins, silicates, amorphous carbon, and nanophase iron, but for specific effective grain sizes. Indeed, for the tholins, the silicates, and the amorphous carbon (respectively $n_r = 1.6, 1.7, 2.0$), HWHM_{cb} is out of the range of the ISS HWHM values for $r_0/\lambda = 0.1$, but a good match can be found for $r_0/\lambda = 0.2$ or for $r_0/\lambda > 1.5$. In the case of nanophase iron ($n_r = 2.9$), the only match possible between HWHM_{cb} and HWHM is for $r_0/\lambda = 0.1$. However, as explained earlier, it seems unlikely that coherent backscattering would be involved either with ice contaminants, or with contaminant grains, but not with both.
- *Intra-mixture.* An intra-mixture consists of small contaminant grains embedded within large ice grains (see Fig. 11). With this type of mixture, photons can be absorbed or scattered before reaching ice/contaminant interfaces. This process is very effective for lowering the albedo. This mixture has been tested for the main rings by Poulet et al. (2003) and Ciarniello (2012). The usual method to calculate the effective real refractive index of an intra-mixture is with the use of the Maxwell Garnett mixing

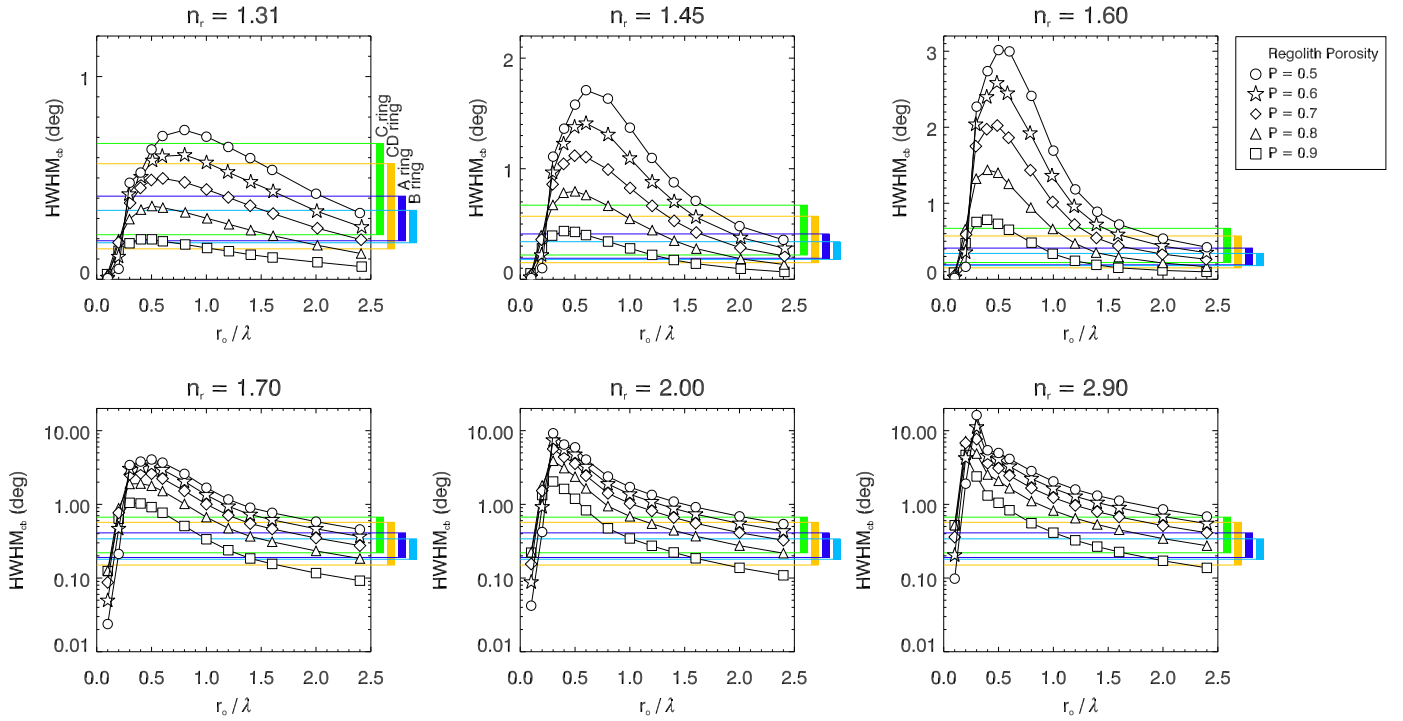


Fig. 10. Coherent backscattering simulations of the angular width (HWHM_{db}) for different values of composition (via the real refractive index n_r), grain size r_0 and the regolith porosity P , using Eqs. (14) and (15). The values $n_r=1.31, 1.45,$ and 1.60 are from Mishchenko (1992, Figs. 1, 2, 3). The ranges of the observed surge width with the ISS data are superimposed for each main ring. Note here that the wavelength is fixed as the refractive index is set to a single value for each panel, meaning that when the ratio r_0/λ varies, it is actually the grain size r_0 that varies.

rule (see e.g. Bohren 1986; Choy 2015):

$$\varepsilon_{\text{eff}} = \varepsilon_1 + \frac{3f_2\varepsilon_1(\varepsilon_2 - \varepsilon_1)}{\varepsilon_2 + 2\varepsilon_1 - f_2(\varepsilon_2 - \varepsilon_1)} \quad (17)$$

$$n_{\text{eff}} = \sqrt{\varepsilon_{\text{eff}}}. \quad (18)$$

where ε_1 and ε_2 are the complex dielectric constants of the matrix material and of the embedded contaminant material, respectively, and f_2 is the fraction of contaminant. Eq. (17) assumes that the inclusions are much smaller than the wavelength.

When comparing the angular widths predicted from the coherent backscattering model using refractive indices of intramixtures to the widths of the observed opposition surge (Table 2), we note that it is not possible to reproduce the main radial variations of the observed opposition surge. This result implies that while the a combination of mixtures can reproduce the shape of the spectra of the main rings, the resulting composition is not in agreement with the prediction of the opposition effect via coherent backscattering. This result appears to be in contradiction with the strong correlation that we found between the opposition surge morphology and the spectral properties. As a consequence, we see that this result can be interpreted two ways: either the intra-mixture is not suitable for the rings, as they were implemented by Poulet et al. (2003) and Ciarniello (2012); or the intra-mixture might be suitable for the rings, but recent studies have shown that the conditions of applicability of approximate effective mixing rules are quite strict and may not be satisfied in the cases considered, see for a review Mishchenko et al. (2016). We will go back to this issue when detailing the analysis for an intimate mixture, as well as the analysis of the grain size and the regolith porosity. However, in the absence of a better solution for the composition, we

will keep the composition proposed by Poulet et al. (2003) and Ciarniello (2012).

- *Intimate mixture.* An intimate mixture consists of contaminant grains mixed with pure water ice grains (see Fig. 11). This type of mixture has been tested for the main rings by Poulet et al. (2003) and Ciarniello (2012). In this type of mixture, the resulting reflectance is a weighted average of the reflectances of the different materials. A reasonable approximation to calculate the effective real refractive index of an intimate mixture is with the use of the “linear mixing rule”. This rule asserts that the refractive index of the mixture is given by the linear average of the indices of the components weighted by their volume fractions:

$$n_{\text{tot}} = f_1 n_1 + f_2 n_2. \quad (19)$$

We have calculated the refractive indices for the main rings using the linear mixing rule seen in Eq. (19) for the abundances of Ciarniello (2012). Note that the abundances of Poulet et al. (2003) provide roughly similar refractive index values as those of Ciarniello (2012), see Table 3. Indeed, $n_{\text{tot}} \sim 1.4$ in the A ring, $n_{\text{tot}} \sim 1.35$ in the B ring, and $n_{\text{tot}} \sim 1.33$ in the C ring. However, slight discrepancies in the n_{tot} values can be noted, and can be attributed to:

- (a) different size distributions: a power law distribution for Ciarniello (2012) and discrete values for Poulet et al. (2003),
- (b) different viewing geometries: at moderate phase angles for Ciarniello (2012, with $\alpha = 17.2^\circ$ for the A ring, $\alpha = 27.0^\circ$ for the B ring, and $\alpha = 37.5^\circ$ for the C ring), and at low phase for Poulet et al. (2003, with $\alpha = 0.6^\circ$ and 4.7° for all rings),
- (c) the location within each ring (Ciarniello (2012) worked on small ring regions of 1000 km length while Poulet et al. (2003) averaged each ring over its entire width).

Table 2

Derivation of the effective refractive index n_{eff} (intra-mixture) for the A, B and C rings and the Cassini Division using the Maxwell Garnett mixing rule – Eq. (17) – and the composition abundances of Ciarniello (2012). In the case of the intimate mixture, we derive the total refractive index n_{tot} using the linear mixing rule of Eq. (19). In both mixtures and in all rings, the porosity is assumed constant ($P = .8$) or is defined by P_{mean} seen in Table 1, and the grain size distribution follows the narrow gamma distribution seen in Eq. (15) with $r_0/\lambda = 1.6$ so that the wavelength is in the range of the ISS CLEAR filters ($\lambda = 0.625 \mu\text{m}$ in the simulations while $\lambda = 0.611 \pm 0.170 \mu\text{m}$ for the NAC and $\lambda = 0.635 \pm 0.143 \mu\text{m}$ for the WAC, see Table 1 of Paper 1). The coherent backscattering angular width HWHM_{cb} from Eq. (14) is numerically calculated for intramixtures and intimate mixture. Mixture 1 in the table is an intimate mixture of Mixture 2 and Mixture 3, with Mixture 2 corresponding to an intramixture of water ice with Triton tholin for all the cases, while Mixture 3 corresponds to either pure amorphous carbon (for the A and B rings) or an intramixture of water ice with amorphous carbon (for the Cassini Division and the C ring). The rings are sorted from left to right to increased values of the observed opposition surge's width from the ISS data. Simple comparison of the radial variations of the coherent backscattering angular width HWHM_{cb} to the ISS surge HWHM shows disagreement at constant porosity (see text for details).

	B ring		A ring		Cassini division		C ring	
Distance to Saturn	102,000–103,000 km		128,000–129,000 km		118,000–119,000 km		80,000–81,000 km	
τ	1.650		0.418		0.133		0.009	
ISS optical surge HWHM	0.22°		0.27°		0.30°		0.33°	
Intimate mixture	Mixture 1		Mixture 1		Mixture 1		Mixture 1	
Abundance	96.5%	3.5%	88%	12%	75%	25%	35%	65%
Intramixture	Mixture 2	Mixture 3	Mixture 2	Mixture 3	Mixture 2	Mixture 3	Mixture 2	Mixture 3
Abundance								
Water ice	99.5%	□	99.6%	□	99.6%	98.4%	99.8%	98.7%
Triton tholin	0.5%	□	0.4%	□	0.4%	□	0.2%	□
Amorphous carbon	□	100%	□	100%	□	1.6%	□	1.3%
Intra-mixture	Mixture 2	Mixture 3	Mixture 2	Mixture 3	Mixture 2	Mixture 3	Mixture 2	Mixture 3
n_{eff}	1.3315	2.00	1.3312	2.00	1.3312	1.3394	1.3306	1.3376
$\text{HWHM}_{\text{cb}}(P = 0.8)$	0.23°	0.36°	0.23°	0.36°	0.23°	0.24°	0.23°	0.24°
$\text{HWHM}_{\text{cb}}(P = P_{\text{mean}})$	0.28°	0.44°	0.35°	0.55°	0.43°	0.44°	0.50°	0.51°
Intimate mixture	Mixture 1		Mixture 1		Mixture 1		Mixture 1	
n_{tot}	1.3549		1.4114		1.3332		1.3352	
$\text{HWHM}_{\text{cb}}(P = 0.8)$	0.25°		0.27°		0.23°		0.23°	
$\text{HWHM}_{\text{cb}}(P = P_{\text{mean}})$	0.30°		0.41°		0.43°		0.51°	

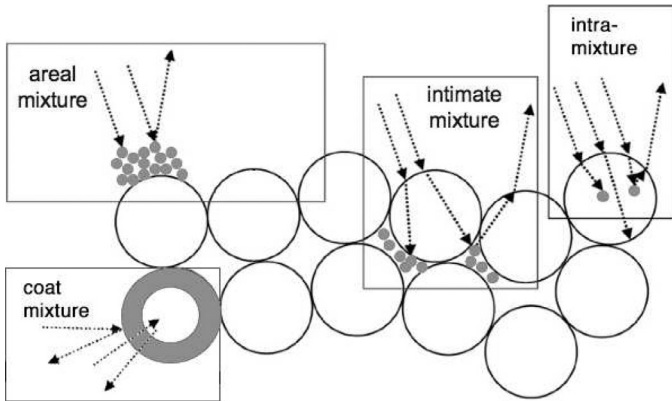


Fig. 11. Schematic representations of two-component mixtures: areal, intimate, intra and coat (adapted from Langevin et al. (2005) and Giuranna et al. (2007)).

Table 3

Derivation of the total refractive index n_{tot} in the case of the intimate mixture using the linear mixing rule of Eq. (19) for the abundances calculated by Poulet et al. (2003) and Ciarniello (2012).

	Poulet et al. (2003)	Ciarniello (2012)
	$n_{\text{tot}}(\lambda = 0.6 \mu\text{m})$	$n_{\text{tot}}(\lambda = 0.6 \mu\text{m})$
A ring	1.3850	1.4114
B ring	1.3476	1.3549
Cassini Division	–	1.3332
C ring	1.3311	1.3352

Then, the angular widths from the coherent backscattering model using refractive indices of intimate mixtures are given in Table 2. When comparing these widths to the width from the ISS data, we see that the radial variations of the observed opposition surge are not reproduced. As a result, the variations of the surge width are matched neither by an intra-mixture, nor by an intimate mixture. We note that while these types of mixing could fit the spectra of the main rings (Poulet et al., 2003;

Ciarniello, 2012), the resulting refractive indices do not reproduce the opposition surge width of the main rings, which is puzzling.

- **Coat mixture.** A coat mixture consists of a layer of contaminated ice covering a core of rock. This concept can occur at two different scales: microscopically, at the regolith grain scale, or macroscopically, at the ring particle scale.

At a microscopic scale, processes such as sputtering can coat individual regolith grains with a super thin film of contaminants so that the regolith grain itself is a structural onion-skin type mixture, e.g. (Hapke, 1986b).

At a macroscopic scale, this coat mixture has been formulated by Déau (2007), and was tested recently on CIRS equinox data by Morishima et al. (2016). The assumption is that the light penetrates deeper into the regolith and reaches the subsequent layers up to the particle core. However, only the light at longer wavelengths should be concerned (i.e. in the thermal infrared), meaning that at optical wavelengths, the coat mixture is not very different from the intimate mixture. Thus, our results for the intimate mixture should be similar for the coat mixture.

4.2.3. Grain size

One of the pillars of the coherent backscattering theory is that it depends strongly on the size of the grains, e.g. Wolf and Maret (1985). The coherent backscattering theory predicts that the angular width of the surge increases with increasing grain size when the grain size is less than half of the wavelength ($r_0 < \lambda/2$), and then increases with increasing grain size for larger grain sizes ($r_0 > \lambda/2$). In Eq. (14), the grain size is given by the effective radius of a gamma size distribution. However, other size distributions are possible, such as the power law (used in Paper 2) or a log-normal distribution. We propose to study each parameter of the size distribution (effective size, width of the size distribution, and type of size distribution) to assess the impact of the grain size on HWHM_{cb} .

- *The effective radius*

The role of the effective radius on HWHM_{cb} is quite self-explanatory. As previously seen in Figs. 8 and 10, HWHM_{cb} increases up to $r_0/\lambda < 1/2$, and then decreases with increasing r_0/λ with a shape similar to a gaussian. To test a more realistic case, we have used the porosity P_{mean} in Table 1, $\lambda = 0.6\mu\text{m}$, and the composition of Ciarniello (2012) for the intimate mixture seen in Table 2. For this test, we use the narrow gamma size distribution seen in Eq. (15).

The simulations are presented in Fig. 12, where one can see that the gaussian-shape size-dependence of HWHM_{cb} is easily reproduced. In addition, as the selected composition is given for small specific regions in the main rings, we can compare the simulations to the ISS data to derive a size that allows them to match. It turns out that for a constant porosity, two possible effective sizes r_0 allow a match between HWHM_{cb} and HWHM derived from the ISS data: either very small sizes ($r_0 \sim 0.1\mu\text{m}$) for $r_0 < \lambda$, or micron-sized values for $r_0 > \lambda$. These sizes are reported in Table 4. In Fig. 12, for $r_0 > \lambda$, it can also be seen that r_0 is larger in the C ring (1.33 μm) than in the B ring (1.22 μm). This result is new because the grain sizes are usually larger in the B ring than in the C ring (Poulet et al., 2002; Filacchione et al., 2012; Hedman et al., 2013; Déau, 2015). The origin of this difference lies in the assumption of the regolith porosity. In all of the previously cited works, the regolith porosity was assumed constant across the rings, whereas in the present case, the porosity significantly varies with P_{mean} seen in Table 1. To demonstrate that larger sizes can be found in the B ring, we have used a constant porosity of $P = 0.8$ in Fig. 12. The gaussian shape is very similar to the one for $P = P_{mean}$, but the values of HWHM_{cb} are significantly smaller, except in the B ring where P_{mean} is close to 0.8 (see Table 1). As expected, the effective size r_0 is larger in the B ring (1.11 μm) and smaller in the C ring (0.75 μm) when $r_0 > \lambda$. This result provides a strong explanation for a long-term result concerning the sizes of the ring regolith, and how the degeneracy between model parameters can be removed.

Finally, a third and last case is presented in Fig. 12, the case where r_0 is close to $\lambda/2$. In this specific case, HWHM_{cb} is maximum and equals HWHM from the ISS data. We have run numerous simulations to find the porosity that allows the match $\text{HWHM}_{cb} = \text{HWHM}$. This porosity, called P_{max} , has the following values: 0.918 in the B ring, 0.926 in the A ring, 0.865 in the Cassini Division, and 0.850 in the C ring. These values are, however, out of the possible range first derived with a composition of $n_r = 1.31$ (see the range of values in Table 1). In addition, it can be noted that these values are not compatible with three “canonical” surface states from the restitution coefficient inversion (Fig. 9b).

This result suggests that finding an acceptable range of values for all the input parameters of the coherent backscattering model should be an iterative process. As a summary, there are three ways to interpret the role of the effective grain size:

- the effective radius is about $\lambda/2$, and in this case HWHM_{cb} is maximum with $P = P_{max}$. However, this should be very coincidental and unlikely to have the effective grain size of the ring regolith about $\sim \lambda/2$.
- the effective radius is less than $\lambda/2$; in this case the porosity does not count as the retrieval of the r_0 leads to a similar value ($r_0 \sim 0.1\mu\text{m}$, see Fig. 12 and Table 4).
- the effective radius is greater than $\lambda/2$, and then the porosity plays a role: (a) if the porosity is constant in all the rings, the effective radius is maximum in the B ring, and minimum in the C ring. This is a general result found in virtually all the previously published spectroscopic works on the rings, see e.g. (Filacchione et al., 2012, their Table 6)

and Hedman et al. (2013, their Fig. 17) or (b) if the porosity varies as indicated in Table 1, the situation is reversed and the C ring has the largest effective grains.

- *The size range*

In the previous section, we focus on the effective radius of the gamma size distribution seen in Eq. (15); however, in most ring studies, the power law is the mostly favored size distribution because it is easy to handle and requires only the boundaries of the distribution (r_{min} and r_{max}) as well as the power law index q , which is often set to -3 , see a review in Paper 2. The formula for the power law size distribution with an index -3 is given by:

$$n(r) = \frac{2r_{min}^2 r_{max}^2}{r_{max}^2 - r_{min}^2} r^{-3} \quad (20)$$

for $r_{min} \leq r \leq r_{max}$, see Hansen and Travis (1974). Note that Eq. (20) is the exact formula for a power law of -3 while most studies used the approximate form without the normalization coefficient (see e.g. Eq. (1) of Paper 2). The effective grain size and the variance for $q = -3$ are:

$$r_{eff} = \frac{r_{max} - r_{min}}{\ln(r_{max}/r_{min})}, \quad (21)$$

$$v_{eff} = \frac{r_{max} + r_{min}}{2(r_{max} - r_{min})} \ln\left(\frac{r_{max}}{r_{min}}\right) - 1. \quad (22)$$

Note that the effective grain size formula can also be found for various power law indices in Table 3 of Déau (2015, Paper 2). As can be seen with Eqs. (21) and (22), the effective radius and the variance are determined by the choices of r_{min} and r_{max} . It is here proposed to explore the range of values for these two parameters in order to assess their impact on the determination of HWHM_{cb} . In Fig. 13, three methods are tested: first, the variance is kept constant (Fig. 13a), second, r_{min} is kept constant (Fig. 13b), and third, r_{max} is kept constant (Fig. 13c). The resulting variations of HWHM_{cb} are explained below:

- when the variance is kept constant, HWHM_{cb} is basically an increasing function of decreasing r_{eff} , see Fig. 13a. In this set of simulations, r_{min} varies from 10 μm to 0.2 μm and r_{max} varies from 60 μm to 1 μm . Large values of r_{min} and r_{max} ($> 10\mu\text{m}$) lead to very small HWHM_{cb} values of about 0.001° , while small values of both r_{min} and r_{max} ($< 1.5\mu\text{m}$) allow HWHM_{cb} to match the angular width of the ISS data.
- when the minimum radius r_{min} is kept constant and fixed at 0.1 μm (Fig. 13b), HWHM_{cb} varies the same way as in the case of a constant variance. Even with $r_{min} = 0.1\mu\text{m}$, large values of r_{max} still lead to extremely small values of HWHM_{cb} that are not compatible with the ISS data. Therefore, r_{max} values of 1 μm (or smaller) are necessary to reach similar values of angular width from the ISS data.
- when r_{max} is kept constant, HWHM_{cb} is an increasing function of increasing r_{eff} , which is unusual in light of the two former cases. Here, the minimum radius r_{min} varies from 0.01 μm to 1 μm while r_{max} is kept constant at 5 μm (Fig. 13c). These very extreme values of radii for both r_{min} and r_{max} are responsible for the distinct behavior of HWHM_{cb} . In addition, it can be noted that HWHM_{cb} cannot reach values as high as the ones from the ISS data, even though the effective radius is about 1 μm , a value that was still possible in the case of a constant variance (Fig. 13a) or even in the case of the gamma size distribution (see Table 4 and Fig. 12). This demonstrates that setting r_{max} to very large values (e.g. 5 μm) does not produce a significant peak width.

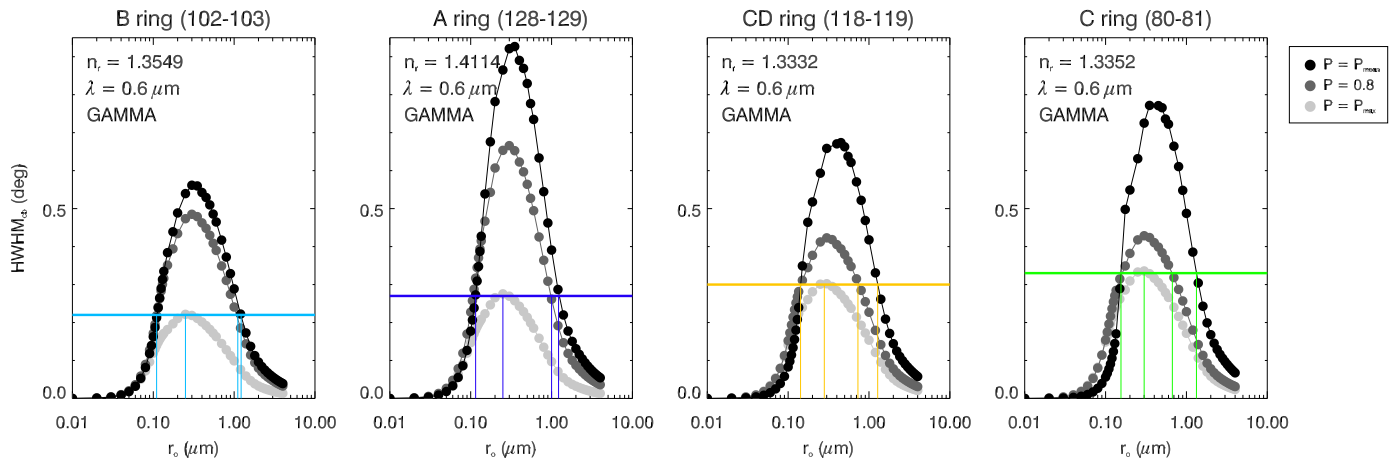


Fig. 12. Derivation of the effective grain size value from the match of the coherent backscattering angular width HWHM_{cb} from Eqs. (14) and (15) and the ISS surge HWHM for 4 features in the main rings, the same for which the refractive index $n_r = n_{tot}$ was derived in Table 2. The other input parameters of the simulations are: $\lambda = 0.6 \mu\text{m}$ and $P = 0.8$ (or $P = P_{mean}$ from Table 1). The vertical solid line represents the value of HWHM from the ISS data. It appears that for each ring, four grain sizes can be derived from the intersection between HWHM_{cb} and HWHM. These values are derived from the intersection of the vertical lines and the horizontal line and are reported in Table 4.

Table 4

Effective grain size values from the match of the coherent backscattering angular width HWHM_{cb} from Eqs. (14), (15), and (20) and the ISS surge HWHM seen in Fig. 12. The other input parameters of the simulations are: $\lambda = 0.6 \mu\text{m}$, $P = .8$ (or $P = P_{mean}$ from Table 1 or $P = P_{max}$ with $P_{max} = 0.918, 0.926, 0.865, 0.85$ for the B, A, CD, C rings respectively) and $n_r = n_{tot}$ from Table 2.

	Gamma size distribution - Eq. (15)				Power law size distribution - Eq. (20)
	$r_0 < \lambda$	$r_0 \approx \lambda/2$	$r_0 > \lambda$		$r_{eff} > \lambda$
	$P = .8$ or P_{mean}	$P = P_{max}$	$P = .8$	$P = P_{mean}$	$P = P_{mean}$
A ring	0.115 μm	0.25 μm	1.00 μm	1.22 μm	0.2–1.2 μm
B ring	0.110 μm	0.25 μm	1.11 μm	1.22 μm	0.2–1.2 μm
Cassini Division	0.143 μm	0.28 μm	0.73 μm	1.28 μm	0.3–1.3 μm
C ring	0.155 μm	0.30 μm	0.67 μm	1.33 μm	0.3–1.6 μm

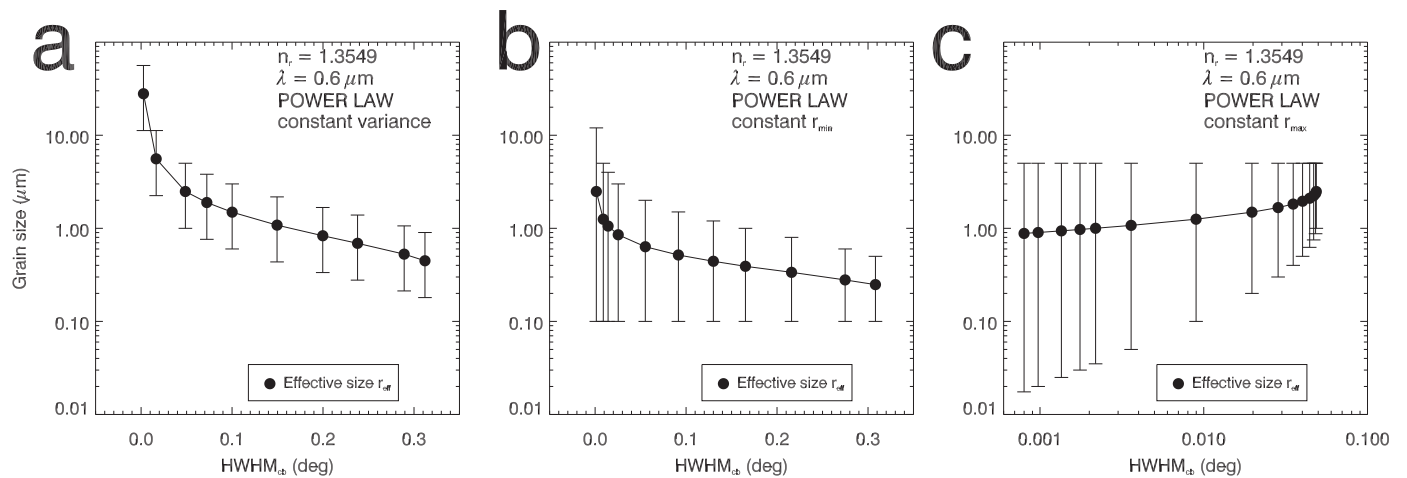


Fig. 13. Variation of HWHM_{cb} from Eq. (14) and (20) using various values for r_{min} and r_{max} , and consequently various values of r_{eff} , see Eq. (21). The other input parameters of the simulations are: $\lambda = 0.6 \mu\text{m}$, $P = P_{mean}$ from Table 1, and $n_r = n_{tot}$ from Table 2 for the B ring region between 102,000 km and 103,000 km. Panel a represent the results of simulations with a constant variance, Panel b with a minimum cutoff r_{min} set to be constant, and Panel c with a maximum cutoff r_{max} set to be constant.

As a result, too small values of r_{min} or too large values of r_{max} can prevent HWHM_{cb} from reaching the level of HWHM values of the ISS data. This can allow us to constrain the grain size range of the four specific regions in the main rings seen in Table 2.

In Fig. 14, we represent the results of several batches of simulations for HWHM_{cb} , with each batch corresponding to a fixed value of r_{min} and a varying value of r_{max} . These simulations indicates that very small values of the lower cutoff

(i.e. $r_{min} = 0.035 \mu\text{m}$) and large values of the lower cutoff (i.e. $r_{min} = 3.5 \mu\text{m}$) do not allow HWHM_{cb} to reach the level of HWHM from the ISS data. For the higher cutoff (i.e. r_{max}), values larger than $2 \mu\text{m}$ do not allow a match between HWHM_{cb} and HWHM. Therefore, one can conclude that $r_{min} > 0.035 \mu\text{m}$ and $r_{max} < 2 \mu\text{m}$ are the two conditions necessary to allow a match between HWHM_{cb} and HWHM. In detail, the range of values of effective radius r_{min} is given for each ring region in Table 4.

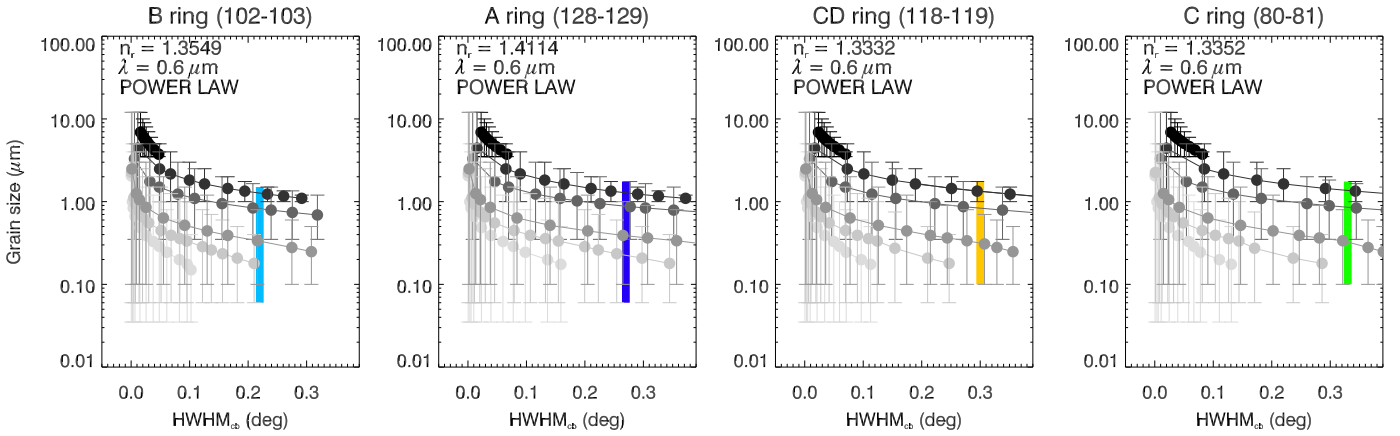


Fig. 14. Derivation of grain size ranges from the comparison of HWHM from the ISS data and HWHM_{cb} from Eqs. (14) and (20) using various values for r_{min} and r_{max} . The dots represent various values of r_{eff} , see Eq. (21), color-coded with different values of r_{min} . The other input parameters of the simulations are: $\lambda = 0.6 \mu\text{m}$, $P = P_{\text{mean}}$ from Table 1, and $n_r = n_{\text{ref}}$ from Table 2. (For interpretation of the references to color in this figure legend, the reader is referred to the web version of this article).

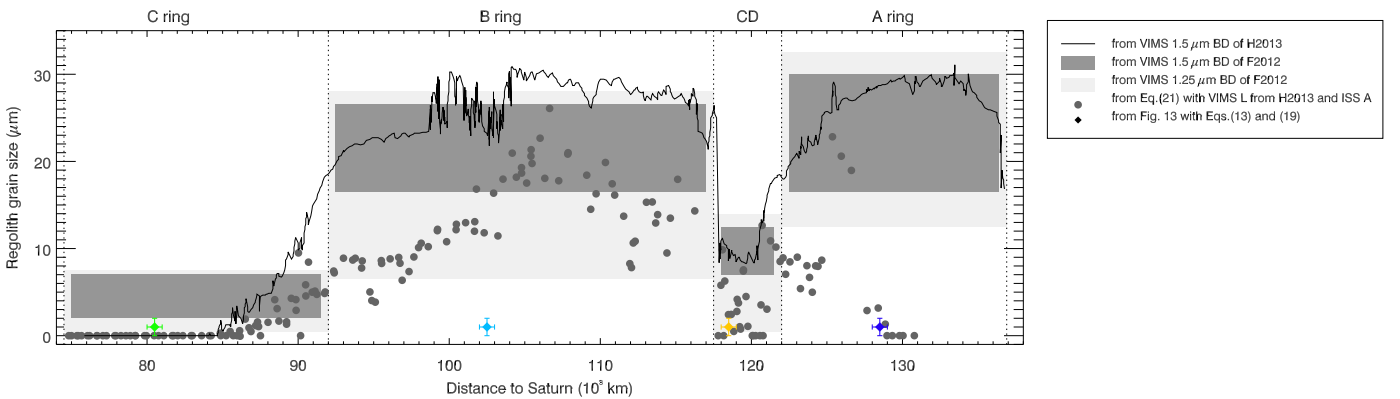


Fig. 15. Comparison of grain radius derived by the present study using the match between HWHM_{cb} from the numerical simulations and HWHM from the ISS data, and the grain radius derived by other studies. These other values are the grain radii from Filacchione et al. (2012, Table 6) using an inversion based on laboratory data to convert the 1.25 μm and 1.5 μm water ice band depths to grain sizes. We have also applied this inversion to the 1.5 μm water ice band depth of Hedman et al. (2013), here in solid line. The grain size d from Eq. (23) is calculated from L , the scattering length derived from VIMS data by Hedman et al. (2013) and A , the surge amplitude from ISS data and seen in Paper 1 and Fig. 2.

• Comparison with other sizes

We propose here a brief comparison of the grain sizes from other studies, by focusing particularly on the grain sizes derived from the Cassini VIMS water ice band depths with the method of Filacchione et al. (2012). These values are reported by Filacchione et al. (2012, Table 6) using an inversion based on laboratory data to convert the 1.25 μm and 1.5 μm water ice band depths to grain sizes. As these values are averaged for each ring (see Fig. 15), to have a sense of the radial variations of the grain size, we have used the inversion method (Filacchione et al. (2012, Fig. 6) with the VIMS 1.5 μm band depths of Hedman et al. (2013) from the observation VIMS_008_RI_RDHRCOMP. We first note that the grain sizes from the 1.5 μm band depths of Filacchione et al. (2012) and Hedman et al. (2013) are compatible, which proves that the grain size derivation with this inversion method is not very sensitive to the viewing geometry. The comparison of the grain radii from the VIMS data and from the HWHM matching method seen in the previous section (Fig. 14) provides a good agreement between the values, except in the A and B ring, see Fig. 15. Moreover, in the C ring and the Cassini Division, there is only an agreement between the sizes from Fig. 14 and the VIMS grain sizes from the 1.25 μm water ice band depths. Another way to see this agreement is to note that the C ring and the Cassini Division grain sizes from the 1.25 μm water ice band

depths are very small, which is always the case in the coherent backscattering simulations of Fig. 14.

To search for clues about the discrepancies between the VIMS grain sizes and the grain sizes from the coherent backscattering simulations, we investigate other grain sizes. Another way to estimate grain sizes is to use the coherent backscattering theory of Shkuratov et al. (1999a). In the theory of Shkuratov et al. (1999b) (where the grain size d is wavelength-sized or larger), the amplitude of the coherent backscattering peak decreases with increasing grain size. This result has been approximated by Poulet et al. (2002) as:

$$A_{cb} = 1 + \frac{\exp(-d/L)}{2}, \quad (23)$$

with L the scattering length within the material. Hedman et al. (2013) derived a scattering length from the spectral Shkuratov et al. (1999a) model. This length can be approximated to the parameter L of the Shkuratov et al. (1999b) opposition effect model that has been used in Paper 2. Then using Eq.(23), the grain size d can be derived by assuming that $A_{cb} \approx A$, with A the surge amplitude from the ISS data seen in Fig. 2 and obtained in our Paper 1.

In order to have the smallest opposition amplitudes with the coherent backscattering theory, as in the ISS observations (Fig. 2), the A and B rings must have the largest grains. This trend, depicted in Fig. 15, is very similar to the one from the

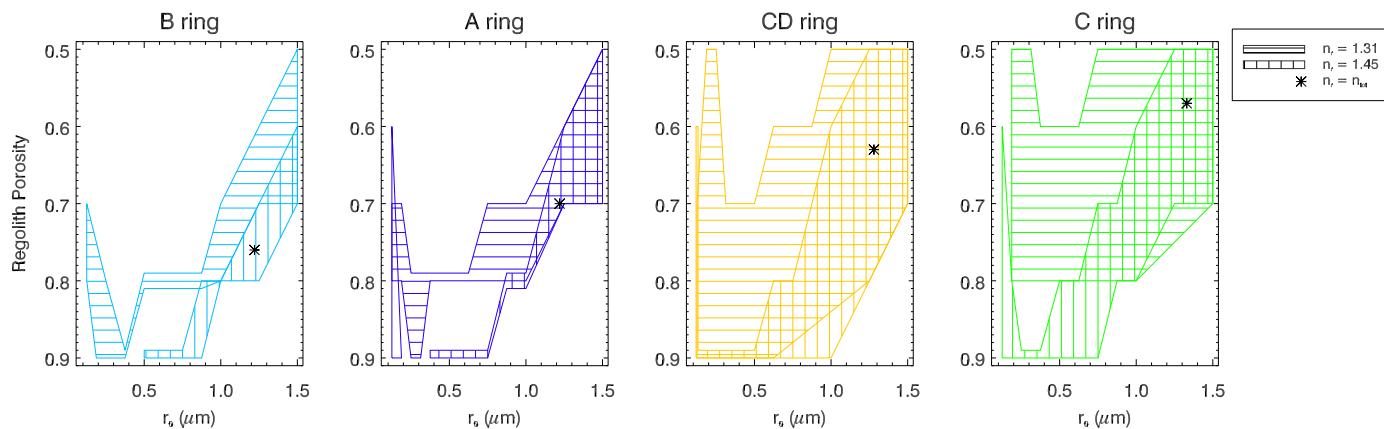


Fig. 16. Range of possible values for the regolith porosity and effective grain size r_0 from the comparison of HWHM and HWHM_{cb} , where HWHM is the angular width of the opposition peak from the ISS data at ($\lambda \sim 0.6$) and HWHM_{cb} is the coherent backscattering angular width from the simulations of Mishchenko (1992) seen in Fig. 10 using Eq. (14) with $\lambda = 0.625 \mu\text{m}$. Note that r_0 is the effective grain size for the gamma size distribution seen in Eq. (15). Hatched regions are the parameter space where there is a match between HWHM and HWHM_{cb} seen in Fig. 10, while the star symbol corresponds to the parameter space seen in Table 2 for the intimate mixture and the real refractive index n_{tot} .

VIMS sizes, except for the A ring. We thus conclude that the size dependence of the coherent backscattering amplitude is compatible with the grain size values in the B and C rings and the Cassini Division. Interestingly, the sizes from Eq. (23) are also compatible with the sizes from the coherent backscattering simulation seen in Fig. 14. From these various agreements, we can conclude that the B ring has larger grains and might be in the geometric optics domain where the grain size is far larger than the wavelength. In the C ring and the Cassini Division, the Mie scattering domain might be valid. Finally, in the A ring, the disagreement between the VIMS sizes on one hand and the coherent backscattering theories on the other hand could be the consequence of both scattering regimes being valid for this ring.

4.2.4. Regolith roughness

Only a few studies have investigated the role of roughness on coherent backscattering. Two kinds of surface roughness can be defined: one with large height variations and steep slopes and the other with only small height variations (Muinonen, 1994). Among the recent studies about the effect of the roughness on the opposition effect (e.g., Zubko et al. (2007); Grynko and Pulbere (2009)), the work of Parviainen and Muinonen (2007, 2009) seems to show that the two types of roughness should have similar effects on the opposition effect morphology. However, the main trends are not clear in these studies.

4.2.5. Summary

In summary, we conclude that the effective grain size, the regolith porosity, and the composition all have an impact when reproducing the angular width of the opposition effect, via the coherent backscattering theory. However, these three parameters do not impact HWHM_{cb} equally. Indeed, using the results of the matching between the HWHM and HWHM_{cb} from Figs. 10 and 12 that we summarize here in Fig. 16, it can be concluded the composition should not have a primary role, and it is actually the regolith porosity and the effective grain size that are preponderant. Indeed, it is possible to find an agreement between the HWHM and HWHM_{cb} for various values of refractive indices, while the regolith porosity and the effective grain sizes are restricted to specific ranges.

4.2.6. Limitation of the approach and future work

In this section, we have used the coherent backscattering model of Mishchenko (1992) to seek for clues on origin of the strong cor-

relation between opposition surge morphology and spectral properties (in particular water ice band depths). However, it must be noted that this model has strong assumptions, and to be cautious with the interpretation of the simulation results, it is important to provide an assessment of the weaknesses and limits introduced by the simplifications that Mishchenko (1992) adopted to make his coherent backscattering model practical enough for computation without violating Maxwell's equations. Before starting, it is noteworthy to reiterate the current standard designation for entities that make up Saturn's rings: particles are the big, macroscopic objects detected by stellar occultations (Zebker et al., 1985; Showalter and Nicholson, 1990; French and Nicholson, 2000; Jerousek et al., 2016), grains belong to the regolith that covers the ring particles (Poulet et al., 2002).

- The fundamental pillar of coherent backscattering is that the dominant scatterers are too small to fall within the geometric optics domain and too transparent to cast shadows. To make coherent backscattering observable (i.e., to make the angular width of its manifestations sufficiently large), they must be comparable to or smaller than the wavelength of light. For example, at optical wavelengths, it means that the scatterers are sub-micron-sized grains (Mishchenko, 1992), whereas at longer wavelengths like the radio domain, the scatterers are centimeter-sized ring particles (Mishchenko and Dlugach, 2009).

In most planetary surfaces, such small regolith grains are not easy to interpret when modeling optical opposition effects. Indeed, considering previous works on lunar regolith grains (Hapke et al., 1993), interplanetary dust grains (Brownlee et al., 1980; Greenberg and Hage, 1990), and captured cometary grains (Tuzzolino et al., 2004), there are indications that micro-scaled structures on airless planetary bodies are most likely to be micro-structural irregularities on the surfaces and within the regolith grains themselves, and those structural imperfections might act as scatterers in their own right. However, in the case of the rings, we have evidence that submicrometer-sized grains exist for quite some time now. Observed by Voyager and Cassini in the outer B ring, levitated dust grains create radial patterns called spokes, e.g. Smith et al. (1981), Mitchell et al. (2013), which are well modeled by radiative transfer theory that includes micron-sized grains, (Doyle et al., 1989; Doyle and Grun, 1990; McGhee et al., 2005; D'Aversa et al., 2010). In the present work, we have just assumed that grains as small as the spoke dust are present in the other main rings.

- [Mishchenko \(1992\)](#) assumed that the regolith porosity provides a measure of the separation between the grains forming the outer regolith layer. Consequently, the regolith porosity from the model should not be a representation of porosity of the ring particle up to its core. Indeed, assuming that the porosity of each regolith layer is uniform throughout the ring particle interior might not be correct, as in-situ Apollo measurement showed in the case of the Moon that as we go deeper in the lunar regolith, the porosity decreases ([Carrier et al., 1973](#)).
- In [Section 4.2.2](#), we defined several mixtures that are often used for ring spectroscopic modeling: the areal mixture, the intra-mixture, the intimate mixture, and the coat mixture, see [Fig. 11](#). So far, the rings are better modeled spectroscopically with intra and intimate mixtures, see [Poulet et al. \(2003\)](#) and [Ciarniello \(2012\)](#), therefore we have calculated the effective refractive indices from these studies in [Table 3](#) using the very simple mixing [Eqs. \(17\) and \(19\)](#). We have injected these effective refractive indices onto [Mishchenko \(1992\)](#)'s model and derived coherent backscattering angular widths. However, the model assumes an homogeneous medium. In [Section 4.2.2](#), we have argued that using effective refractive index is an acceptable assumption considering the random nature of the multiple scattering involved in coherent backscattering. Also, considering that we are using a single wavelength in the present study, uncertainties on composition introduced by the mixing rules might not have a large impact. Future modeling of coherent backscattering should include mixtures that are directly handled by the model itself, e.g. ([Lasue et al., 2007; 2009](#)).
- [Mishchenko \(1992\)](#) adopted perfectly smooth spheres to model regolith grains. However, for highly comminuted regolith grains, especially those made of volatile materials that have been bombarded by radiation and energetic particles, grains' surface might present micro-structural damage or imperfections: micropits, cracks, embedded contaminants, inclusions, crystal defects etc. These micro-structures are not fully modeled yet, although the recent work of [Mishchenko and Dlugach \(2012\)](#) and [Dlugach and Mishchenko \(2015\)](#) has analyzed the behavior of the integral and angular scattering characteristics of spheres with, respectively, surface minerals/soot and inclusions. As a result, using smooth grains is somewhat geologically unrealistic, but it is useful for exploring the behavior of the coherent backscattering opposition effect in a semi-quantitative way.
- From [Figs. 2, 4](#), and [A.1](#), we have shown that A and HWHM follow the same trends with radial distance to Saturn and VIMS spectral properties. We have previously argued that this result could imply that A and HWHM are likely to be controlled by the same mechanisms. However, this viewpoint is too simplistic for the following reasons. It is clear that A and HWHM are controlled by the same mechanisms responsible for producing the opposition peak (since they both describe the shape of this peak, rather than because they show the identical trends), and coherent backscattering is dominant (since the opposition peak measured in Saturn's rings is narrow, while shadow hiding produces a wider peak). In the mean time, the trends in the behavior of the peak's amplitude and angular width may differ in dependence on which of the properties of the scattering medium are varied and what the other properties are. Indeed, the growth of the interparticle distance (i.e., the interference base) considered by [Mishchenko](#) makes both the amplitude and the width of the peak smaller. However, the change in the other properties of the medium may produce the effects of different signs on A and HWHM even for the medium, where coherent backscattering plays a major role in the opposition effect. For example, for smaller particles or more porous media, the opposition surge becomes higher and narrower, while the consequences of changes in the real and imaginary parts of the re-

fractive index may vary depending on the porosity and particle size ([Lumme and Penttilä, 2011; Dlugach et al., 2011; Tishkovets and Petrova, 2013; 2017](#)). Future simulations with both amplitude and angular width as outputs and comparison with A and HWHM from the data (and not only HWHM as is done here) will greatly improve our understanding of the regolith properties' interplay.

- Finally, to provide possible constraints for surface regolith properties, we have fit results from the coherent backscattering model of [Mishchenko \(1992\)](#) to yield the HWHMs derived from the data. However, we note that the HWHM values derived from the ring phase curves vary from one study to another, especially in the HST studies ([Poulet et al., 2002; French et al., 2007](#)). Discrepancies between A and HWHM values could be a wavelength effect. Indeed, from the coherent backscattering theory, HWHM_{cb} significantly varies with the wavelength, therefore it is expected that HWHM might vary as well, if believed to be caused by coherent backscattering. In the present paper, we are using broadband images with the CLEAR filters ($\lambda = 0.611 \pm 0.170 \mu\text{m}$ for the NAC and $\lambda = 0.635 \pm 0.143 \mu\text{m}$ for the WAC) whereas previous HST studies ([Poulet et al., 2002; French et al., 2007; Salo and French, 2010](#)), used bandpasses with $\Delta\lambda$ ranging from 0.037 to 0.176 μm , see [Table II of Cuzzi et al. 2002](#). We will compare HWHM values from Cassini and HST data in future work. Another effect could be the use of different morphological models. In theory, when the data have a good phase angle sampling, including very small phase angles, all morphological models tend towards the same set of values. However, when the phase angle sampling is poor and/or when the phase curve does not cover the smallest phase angles, all models will extrapolate the data to obtain the best fit, and some models are better doing it than others. For example, with Paper's 1 dataset and using the linear-exponential model, see [Eq. \(3\)](#) in [Paper 1](#), [Déau \(2007\)](#) noted a factor of two smaller HWHM for a C ring phase curve with a typical phase angle coverage (0.025° – 25°) and the same phase curve with part of the surge removed (omitting the data at phase angles less than 0.3°), see [Figure F.2, page 371](#). This result is confirmed with the discrepancy between two HST studies where the phase angle coverage varies: with the phase curves of [Poulet et al. \(2002\)](#) having a mediocre phase angle coverage at low phase (0.3 – 6°), the C ring's HWHM is about 0.67° at $0.555 \mu\text{m}$, see their [Table II](#), whereas in the study of [French et al. \(2007\)](#), with better coverage at low phase (0.012 – 6°), the C ring's HWHM is about 0.10° at $0.555 \mu\text{m}$, see their [Table 5](#). Although the ratio between the two HWHM inferred from HST data is closer to 7 than to 2, we note that if these HST studies would have used our methodology to constrain the regolith properties, the inferred values would have been different from ours.

5. Conclusions

We summarize the main conclusions of our work:

- ① One of our main concerns from previous works on the ring opposition effect is the nature of the mechanism involved. From the previous work on the elevation angle dependence of observed opposition effect seen in the HST datasets, ([Salo and French, 2010](#)), there is evidence that coherent backscattering, regolith shadow hiding, and interparticle shadowing are likely to be present to form the ring opposition effect. However, since the phase curves analyzed in [Paper 1](#) correspond to rather high elevation angles (see [Fig. 1](#) of [Paper 2](#)), the contribution from mutual shadowing

is in the current case less than that due to the contribution of coherent backscattering and regolith shadow hiding.

From the present work, which shows the strong correlation between the surge amplitude and the water ice band depth at 1.5 μm (Fig. 4a), one can conclude that the mechanism that affects the water ice band depth observed by VIMS at moderate phase angle is also acting in the opposition surge seen by ISS. This correlation indicates that this common mechanism must be wavelength dependent, as the cited quantities were measured at various wavelengths. So far, there is evidence that this mechanism is coherent backscattering because only coherent backscattering can act on water ice bands and the opposition surge at the same time, see Mishchenko et al. (2006), Kolokolova et al. (2010) and Muinonen et al. (2012). Quite importantly, coherent backscattering caused by microscopic regolith grains is the only optical mechanism that has been shown to cause simultaneously both the spike-like photometric and the polarimetric opposition effects observed for Saturn's rings (Lyot, 1929; Mishchenko, 1993; Rosenbush et al., 1997; Mishchenko et al., 2009). Also, because the alternatives (regolith shadow hiding and interparticle shadow hiding) are wavelength-independent, see Shkuratov et al. (1999a) and Salo and French (2010), coherent backscattering appears as the only valid candidate. To be exact, there is one more wavelength-dependent mechanism that may contribute to the opposition effect (the near-field mechanism, which operates primarily in densely-packed, low-albedo media, see the Introduction). However, its contribution should not be significant here because Saturn ring's regolith is not likely to be a densely packed medium (indeed elastic collisions and low impact velocities between ring particles have been established to rule the ring layer, and these dynamical constraints seem to favor porous regoliths).

- ② As the regolith albedo and spectral properties are related to the grain size, the porosity and the composition, we have tried to assess which of these regolith properties is preponderant in the surge morphology by numerically calculating the variations of the coherent backscattering angular width HWHM_{cb} with Mishchenko (1992)'s model. We have found that the grain size is the most obvious candidate, as it easily allows a good match between HWHM_{cb} and the width of the observed peak (Figs. 12 and 14); however, the regolith porosity cannot be excluded at this point (Fig. 8). Also, we have found the origin of a persistent result in previous spectroscopic studies that consists in regolith grain sizes being larger in the B ring than in the C ring (Poulet et al., 2002; Filacchione et al., 2012; Hedman et al., 2013; Déau, 2015). The origin of this difference lies in the assumption of constant regolith porosity. If the porosity is not constant for these rings, it is possible to obtain a different result, and even the opposite result, see Table 4.
- ③ By looking at the strength of the correlations between the surge morphology and the spectral properties, we have been able to show that some spectral properties are more strongly correlated with the opposition effect than others. For example, the 2.0 μm water ice band depth is strongly correlated with the surge amplitude in the C and B rings (Fig. 4a). For the same rings, the correlation is less strong for the near infrared spectral slope (Fig. 4c). In contrast, the correlation is less clear between the surge amplitude and the near ultraviolet spectral slope (Fig. 4b). Indeed, the C ring points do not appear continuous in the (A, S_{NUV}) parameter space but still follow a quite linear correlation. By contrast, the B ring points form a cloud, which means that both A and S_{NUV} are weakly correlated (Fig. 4b). As a result, it seems justified to

infer that the physical properties of the regolith vary ring-by-ring.

However, our study showed that the interpretation of grain sizes may not be straightforward. In airless and magnetized environments such as Saturn's surroundings, it is easy for tiny grains to clump into larger aggregate grains that can have highly complex shapes (Déau, 2014) or even be welded like lunar agglutinates (McKay et al., 1986). There are now a large group of studies of light scattering by densely packed discrete random media composed of clusters (see, Tishkovets and Petrova, 2013; 2017) and by finite multi-particle ensembles (e.g., Zubko et al., 2008; Lumme and Penttilä, 2011; Dlugach et al., 2011). Such sophisticated models coupled with multi-wavelength observations of the rings' opposition effect are necessary to assess the radial variations of the regolith properties.

Acknowledgments

In memory of André Brahic, whose sharp mind and forgiving spirit will never be forgotten. This work was funded by the Cassini Project, through grants issued by the Jet Propulsion Laboratory, California Institute of Technology under contract with NASA. MIM was sponsored by the NASA Remote Sensing Theory Program. PH gratefully acknowledges support from NASA Planetary Geology and Geophysics grant NNX14AN04G. Numerical simulations of the coherent backscattering model were carried out at the Jet Propulsion Laboratory using a Python layer over the Fortran original source code of Mishchenko et al. (1992). Government sponsorship acknowledged. We thank the reviewers for their detailed, and helpful comments.

Supplementary material

Supplementary material associated with this article can be found, in the online version, at [10.1016/j.icarus.2017.12.025](https://doi.org/10.1016/j.icarus.2017.12.025).

References

- Altobelli, N., Spilker, L., Pilorz, S., Brooks, S., Edgington, S., Wallis, B., Flasar, M., 2007. C ring fine structures revealed in the thermal infrared. *Icarus* 191, 691–701.
- Altobelli, N., Spilker, L., Pilorz, S., Leyrat, C., Edgington, S., Wallis, B., Flandes, A., 2009. Thermal phase curves observed in saturn's main rings by cassini-CIRS: detection of an opposition effect? *Geophys. Res. Lett.* 36, L10105.
- Belskaya, I.N., Shevchenko, V.G., 2000. Opposition effect of asteroids. *Icarus* 147, 94–105.
- Bobrov, M.S., 1970. Physical Properties of Saturn's Rings. In: Dollfus, A. (Ed.), Surfaces and interiors of planets and satellites. Academic, New York, pp. 376–461.
- Bohren, C.F., 1986. Applicability of effective-medium theories to problems of scattering and absorption by nonhomogeneous atmospheric particles. *J. Atmos. Sci.* 43, 468–475.
- Brahic, A., 1977. Systems of colliding bodies in a gravitational field. i - numerical simulation of the standard model. *Astron. Astrophys.* 54, 895–907.
- Bridges, F.G., Hatzes, A., Lin, D.N.C., 1984. Structure, stability and evolution of saturn's rings. *Nature* 309, 333–335.
- Bridges, F.G., Supulver, K.D., Lin, D.N.C., Knight, R., Zafra, M., 1996. Energy loss and sticking mechanisms in particle aggregation in planetesimal formation. *Icarus* 123, 422–435.
- Brown, R.H., Baines, K.H., Bellucci, G., Buratti, B.J., Capaccioni, F., Ceroni, P., Clark, R.N., Coradini, A., Cruikshank, D.P., Drossart, P., Formisano, V., Jaumann, R., Langevin, Y., Matson, D.L., McCord, T.B., Mennella, V., Nelson, R.M., Nicholson, P.D., Sicardy, B., Sotin, C., Baugh, N., Griffith, C.A., Hansen, G.B., Hibbits, C.A., Momary, T.W., Showalter, M.R., 2006. Observations in the saturn system during approach and orbital insertion, with cassini's visual and infrared mapping spectrometer (VIMS). *Astron. Astrophys.* 446, 707–716.
- Brownlee, D.E., Pilachowski, L., Olszewski, E., Hodge, P.W., 1980. Analysis of Interplanetary Dust Collections. In: Halliday, I., McIntosh, B.A. (Eds.), Solid Particles in the Solar System. Vol. 90 of IAU Symposium, pp. 333–341.
- Buratti, B.J., Mosher, J.A., Abramson, L., Akhter, N., Clark, R.N., Brown, R.H., Baines, K.H., Nicholson, P.D., Dewet, S., 2009. Opposition Surges of the Satellites of Saturn from the Cassini Visual Infrared Mapping Spectrometer (VIMS). In: Lunar and Planetary Science Conference. Vol. 40 of Lunar and Planetary Institute Technical Report., p. 1738.
- Carrier, W.D., Mitchell, J.K., Mahmood, A., 1973. The Relative Density of Lunar Soil. In: Lunar and Planetary Science Conference. Vol. 4 of Lunar and Planetary Science Conference.

- Chandrasekhar, S., 1960. Radiative Transfer. Dover, New York.
- Choy, T.C., 2015. Effective Medium Theory: Principles and Applications, 2nd Oxford University Press.
- Ciarniello, M., 2012. Theoretical models of the spectrophotometric properties of atmosphereless bodies surfaces in the solar system. INAF-IAPS.
- Ciarniello, M., Capaccioni, F., Filacchione, G., Clark, R.N., Cruikshank, D.P., Cerroni, P., Coradini, A., Brown, R.H., Buratti, B.J., Tosi, F., Stephan, K., 2011. Hapke modeling of rhea surface properties through cassini-VIMS spectra. *Icarus* 214, 541–555.
- Clark, R.N., Cruikshank, D.P., Jaumann, R., Brown, R.H., Stephan, K., Dalle Ore, C.M., Eric Livo, K., Pearson, N., Curchin, J.M., Hoefen, T.M., Buratti, B.J., Filacchione, G., Baines, K.H., Nicholson, P.D., 2012. The surface composition of iapetus: mapping results from cassini VIMS. *Icarus* 218, 831–860.
- Colwell, J.E., Nicholson, P.D., Tiscareno, M.S., Murray, C.D., French, R.G., Marouf, E.A., 2009. The Structure of Saturn's Rings. In: Dougherty, M.K., Esposito, L.W., Krimigis, S.M. (Eds.), Saturn from Cassini-Huygens. Springer, pp. 375–412.
- Cooke, M.L., 1991. Saturn's Rings: Photometric Studies of the c Ring and Radial Variation in the Keeler Gap. Cornell Univ., Ithaca, NY.
- Cuzzi, J., Clark, R., Filacchione, G., French, R., Johnson, R., Marouf, E., Spilker, L., Krimigis, S.M., 2009. Ring particle composition and size distribution. In: Dougherty, M.K., Esposito, L.W. (Eds.), Saturn from Cassini-Huygens, pp. 459–509.
- Cuzzi, J.N., Chambers, L.B., Hendrix, A.R., 2017. Rough surfaces: is the dark stuff just shadow? who knows what evil lurks in the hearts of men? the shadow knows!. *Icarus* 289, 281–294.
- Cuzzi, J.N., Estrada, P.R., 1998. Compositional evolution of saturn's rings due to meteoroid bombardment. *Icarus* 132, 1–35.
- Cuzzi, J.N., French, R.G., Dones, L., 2002. HST Multicolor (255–1042 nm) photometry of saturn's main rings i: radial profiles, phase and opening angle variations, and regional spectra. *Icarus* 158, 199–223.
- Dadic, R., Mullen, P.C., Schneebeli, M., Brandt, R.E., Warren, S.G., 2013. Effects of bubbles, cracks, and volcanic tephra on the spectral albedo of bare ice near the transantarctic mountains: implications for sea glaciers on snowball earth. *J. Geophys. Res. (Earth Surf.)* 118, 1658–1676.
- D'Aversa, E., Bellucci, G., Nicholson, P.D., Hedman, M.M., Brown, R.H., Showalter, M.R., Altieri, F., Carozzo, F.G., Filacchione, G., Tosi, F., 2010. The spectrum of a saturn ring spoke from cassini/VIMS. *Geophys. Res. Lett.* 37, 1203.
- Déau, E., 2007. Saturn's Rings Revisited by the Images of the CASSINI Spacecraft: Dynamical Evolution of the F Ring and Photometric Study of the Main Rings. Université Paris 7 Denis Diderot, Paris. FR.
- Déau, E., 2012. Variations of the apparent angular size of the sun across the entire solar system: implications for planetary opposition surges. *J. Quant. Spectrosc. Radiat. Transf.* 113, 1476–1487.
- Déau, E., 2014. The Size Distribution of Saturn Ring Particles Using N-body Simulations. AGU Fall Meeting Abstracts.
- Déau, E., 2015. The opposition effect in saturn's main rings as seen by cassini ISS: 2. constraints on the ring particles and their regolith with analytical radiative transfer models. *Icarus* 253, 311–345.
- Déau, E., Dones, L., 2018. Cassini/ISS color phase curves of saturn's main rings: color albedos. *Icarus*. *in preparation*.
- Déau, E., Dones, L., Charnoz, S., West, R.A., Brahic, A., Decriem, J., Porco, C.C., 2013. The opposition effect in saturn's main rings as seen by cassini ISS: 1. morphology of phase functions and dependence on the local optical depth. *Icarus* 226, 591–603.
- Déau, E., Dones, L., Rodriguez, S., Charnoz, S., Brahic, A., 2009. The opposition effect in the outer solar system: a comparative study of the phase function morphology. *Planet. Space Sci.* 57, 1282–1301.
- Déau, E., Flandes, A., Spilker, L.J., Petazzoni, J., 2013. Re-analysis of previous laboratory phase curves: 1. variations of the opposition effect morphology with the textural properties, and an application to planetary surfaces. *Icarus* 226, 1465–1488.
- Déau, E., Helfenstein, P., 2018. Cassini ISS broadband photometry of saturn's main rings: i. correlations of ring bulk albedo and optical depth dependence. *J. Geophys. Res.*. *in preparation*.
- Déau, E., Helfenstein, P., Dones, L., West, R., Porco, C., 2018. The opposition effect in saturn's main rings as seen by cassini ISS: 3. improved shadowing parameters and ring layer properties. *Icarus*. *in preparation*.
- Déau, E., Spilker, L.J., Flandes, A., 2016. Re-analysis of previous laboratory phase curves: 2. connections between opposition effect morphology and spectral features of stony meteorites. *Icarus* 272, 149–164.
- Déau, E., Spilker, L.J., Scipioni, F., Mishchenko, M., Flandes, A., Baillié, K., Dones, L., 2018. Phase and spectral effects of major and irregular saturnian satellite surfaces: a clue to ring-satellite interactions? *Icarus*. *in preparation*.
- Dejongio, K., Rodriguez, S., Ferrari, C.C., Brahic, A., 2010. Morphology of enceladus's craters by photometric studies with ISS/Cassini. AGU Fall Meeting Abstracts, A1559+.
- Dlugach, J.M., Mishchenko, M.I., 2015. Scattering properties of heterogeneous mineral particles with absorbing inclusions. *J. Quant. Spectrosc. Radiat. Transf.* 162, 89–94.
- Dlugach, J.M., Mishchenko, M.I., Liu, L., Mackowski, D.W., 2011. Numerically exact computer simulations of light scattering by densely packed, random particulate media. *J. Quant. Spectrosc. Radiat. Transf.* 112, 2068–2078.
- Dollfus, A., 1996. Saturn's rings: optical reflectance polarimetry. *Icarus* 124, 237–261.
- Dones, L., Cuzzi, J.N., Showalter, M.R., 1993. Voyager photometry of saturn's a ring. *Icarus* 105, 184–215.
- Doyle, L.R., Dones, L., Cuzzi, J.N., 1989. Radiative transfer modeling of saturn's outer b ring. *Icarus* 80, 104–135.
- Doyle, L.R., Grun, E., 1990. Radiative transfer modeling constraints on the size of the spoke particles in saturn's rings. *Icarus* 85, 168–190.
- Esposito, L.W., 1979. Extensions to the classical calculation of the effect of mutual shadowing in diffuse reflection. *Icarus* 39, 69–80.
- Esposito, L.W., Lumme, K., Benton, W.D., Martin, L.J., Ferguson, H.M., Thompson, D.T., Jones, S.E., 1979. International planetary patrol observations of saturn's rings. II - four color phase curves and their analysis. *Astron. J.* 84, 1408–1415.
- Fearnside, A., Masding, P., Hooker, C., 2016. Polarimetry of moonlight: a new method for determining the refractive index of the lunar regolith. *Icarus* 268, 156–171.
- Filacchione, G., Capaccioni, F., Ciarniello, M., Clark, R.N., Cuzzi, J.N., Nicholson, P.D., Cruikshank, D.P., Hedman, M.M., Buratti, B.J., Lunine, J.I., Soderblom, L.A., Tosi, F., Cerroni, P., Brown, R.H., McCord, T.B., Jaumann, R., Stephan, K., Baines, K.H., Flamini, E., 2012. Saturn's icy satellites and rings investigated by cassini-VIMS: III - radial compositional variability. *Icarus* 220, 1064–1096.
- Filacchione, G., Capaccioni, F., Clark, R.N., Nicholson, P.D., Cruikshank, D.P., Cuzzi, J.N., Lunine, J.I., Brown, R.H., Cerroni, P., Tosi, F., Ciarniello, M., Buratti, B.J., Hedman, M.M., Flamini, E., 2013. The radial distribution of water ice and chromophores across saturn's system. *Astrophys. J.* 766, 76.
- Filacchione, G., Ciarniello, M., Capaccioni, F., Clark, R.N., Nicholson, P.D., Hedman, M.M., Cuzzi, J.N., Cruikshank, D.P., Dalle Ore, C.M., Brown, R.H., Cerroni, P., Altobelli, N., Spilker, L.J., 2014. Cassini-VIMS observations of saturn's main rings: i. spectral properties and temperature radial profiles variability with phase angle and elevation. *Icarus* 241, 45–65.
- Franklin, F.A., Cook, F.A., 1965. Optical properties of saturn's rings. II. two-color phase curves of the 2 bright rings. *Astron. J.* 70, 704–720.
- French, R.G., Nicholson, P.D., 2000. Saturn's rings II. particle sizes inferred from stellar occultation data. *Icarus* 145, 502–523.
- French, R.G., Verbiscer, A., Salo, H., McGhee, C., Dones, L., 2007. Saturn's rings at true opposition. *Publ. Astron. Soc. Pac.* 119, 623–642.
- Giuranna, M., Hansen, G., Formisano, V., Zasova, L., Maturilli, A., Grassi, D., Ignatiev, N., 2007. Spatial variability, composition and thickness of the seasonal north polar cap of mars in mid-spring. *Planet Space Sci.* 55, 1328–1345.
- Goldreich, P., Tremaine, S., 1978. The velocity dispersion in saturn's rings. *Icarus* 34, 227–239.
- Greenberg, J.M., Hage, J.I., 1990. From interstellar dust to comets - a unification of observational constraints. *Astrophys. J.* 361, 260–274.
- Grynko, Y., Pulbere, S., 2009. Discrete dipole approximation simulations of light reflection from flat non-transparent particles with rough surfaces. *J. Quant. Spectrosc. Radiat. Transf.* 110, 1382–1391.
- Hansen, J.E., Travis, L.D., 1974. Light scattering in planetary atmospheres. *Space Sci Rev* 16, 527–610.
- Hapke, B., 1984. Bidirectional reflectance spectroscopy. III - correction for macroscopic roughness. *Icarus* 59, 41–59.
- Hapke, B., 1986. Bidirectional reflectance spectroscopy. IV - the extinction coefficient and the opposition effect. *Icarus* 67, 264–280.
- Hapke, B., 1986. On the sputter alteration of regoliths of outer solar system bodies. *Icarus* 66, 270–279.
- Hapke, B., 1993. Theory of Reflectance and Emittance Spectroscopy. Cambridge Univ. Press, Cambridge, UK.
- Hapke, B., 2002. Bidirectional reflectance spectroscopy v. the coherent backscatter opposition effect and anisotropic scattering. *Icarus* 157, 523–534.
- Hapke, B., Nelson, R.M., Smythe, W.D., 1993. The opposition effect of the moon - the contribution of coherent backscatter. *Science* 260, 509–511.
- Hatzes, A.P., Bridges, F.G., Lin, D.N.C., 1988. Collisional properties of ice spheres at low impact velocities. *Mon. Not. R. Astron. Soc.* 231, 1091–1115.
- Hedman, M.M., Burns, J.A., Showalter, M.R., Porco, C.C., Nicholson, P.D., Bosh, A.S., Tiscareno, M.S., Brown, R.H., Buratti, B.J., Baines, K.H., Clark, R., 2007. Saturn's dynamic d ring. *Icarus* 188, 89–107.
- Hedman, M.M., Nicholson, P.D., Cuzzi, J.N., Clark, R.N., Filacchione, G., Capaccioni, F., Ciarniello, M., 2013. Connections between spectra and structure in saturn's main rings based on cassini VIMS data. *Icarus* 223, 105–130.
- Helfenstein, P., Veverka, J., Hillier, J., 1997. The lunar opposition effect: a test of alternative models. *Icarus* 128, 2–14.
- Herman, A., Sarrazin, M., Deparis, O., 2014. The fundamental problem of treating light incoherence in photovoltaics and its practical consequences. *New J. Phys.* 16 (1), 013022.
- Jerousek, R.G., Colwell, J.E., Esposito, L.W., Nicholson, P.D., Hedman, M.M., 2016. Small particles and self-gravity wakes in saturn's rings from UVIS and VIMS stellar occultations. *Icarus* 279, 36–50.
- Johnson, P.E., Kemp, J.C., King, R., Parker, T.E., Barbour, M.S., 1980. New results from optical polarimetry of saturn's rings. *Nature* 283, 146–149.
- Kawata, Y., Irvine, W.M., 1974. Models of Saturn's rings which satisfy the optical observations. In: Woszczyk, A., Iwaniszewska, C. (Eds.), Exploration of the Planetary System. IAU Symposium 65, pp. 441–464.
- Khare, B.N., Sagan, C., Arakawa, E.T., Suits, F., Callcott, T.A., Williams, M.W., 1984. Optical constants of organic tholins produced in a simulated titanian atmosphere - from soft x-ray to microwave frequencies. *Icarus* 60, 127–137.
- Khare, B.N., Sagan, C., Thompson, W.R., Arakawa, E.T., Meisse, C., Tuminello, P.S., 1994. Optical properties of poly-HCN and their astronomical applications. *Can. J. Chem.* 72, 678–694.
- Khare, B.N., Thompson, W.R., Cheng, L., Chyba, C., Sagan, C., Arakawa, E.T., Meisse, C., Tuminello, P.S., 1993. Production and optical constraints of ice tholin from charged particle irradiation of (1:6) c2h6/h2o at 77 k. *Icarus* 103, 290–300.

- Kolokolova, L., Buratti, B., Tishkovets, V., 2010. Impact of coherent backscattering on the spectra of icy satellites of saturn and the implications of its effects for remote sensing. *Astrophys. J. Lett.* 711, L71–L74.
- Kuga, Y., Ishimaru, A., 1984. Retroreflectance from a dense distribution of spherical particles. *J. Opt. Soc. Am.* 1, 831–835.
- Lane, A.L., Hord, C.W., West, R.A., Esposito, L.W., Coffeen, D.L., Sato, M., Simmons, K.E., Pomphrey, R.B., Morris, R.B., 1982. Photopolarimetry from voyager 2 - preliminary results on saturn, titan, and the rings. *Science* 215, 537–543.
- Langevin, Y., Poulet, F., Bibring, J.-P., Schmitt, B., Douté, S., Gondet, B., 2005. Evolution of permanent surface water ice at high north latitudes. In: *First Mars Express Science Conference*, 2125 February 2005, European Space Research and Technology Centre (ESTEC), Noordwijk, The Netherlands, pp. 1–14.
- Larson, S., 1984. Summary of optical ground-based E ring observations at the university of arizona. In: Greenberg, R., Brahic, A. (Eds.), *IAU Colloq. 75: Planetary Rings*, pp. 111–114.
- Lasue, J., Levasseur-Regourd, A.C., Hadamcik, E., Alcouffe, G., 2009. Cometary dust properties retrieved from polarization observations: application to c/1995 o1 hale bopp and 1p/halley. *Icarus* 199, 129–144.
- Lasue, J., Levasseur-Regourd, A.C., Hadamcik, E., Renard, J.-B., 2007. Light scattering by coated spheres: experimental results and numerical simulations. *J. Quant. Spectrosc. Radiat. Transf.* 106, 212–224.
- Lumme, K., Irvine, W.M., 1976. Photometry of saturn's rings. *Astron. J.* 81, 865–893.
- Lumme, K., Muinonen, K., Peltoniemi, J., Karttunen, H., Bowell, E., 1987. A possible explanation for anomalously sharp opposition effects. *Bull. Am. Astron. Soc.* 19, 850.
- Lumme, K., Penttilä, A., 2011. Model of light scattering by dust particles in the solar system: applications to cometary comae and planetary regoliths. *J. Quant. Spectrosc. Radiat. Transf.* 112, 1658–1670.
- Lynch, D.K., Mazuk, A.L., Russell, R.W., Hackwell, J.A., Hanner, M.S., 2000. 8- To 13- μm spectra of saturn's a and b rings. *Icarus* 146, 43–47.
- Lyot, B., 1929. Recherches sur la polarisation de la lumiere des planetes et de quelques substances terrestres. *Ann. l'Observ. Paris*, Num. 1, 1–161.
- Mashaal, H., Goldstein, A., Feuermann, D., Gordon, J.M., 2012. First direct measurement of the spatial coherence of sunlight. *Opt. Lett.* 37, 3516–3518.
- McDonald, G.D., Thompson, W., Heinrich, M., Khare, B.N., Sagan, C., 1994. Chemical investigation of titan and triton tholins. *Icarus* 108 (1), 137–145.
- McGhee, C.A., French, R.G., Dones, L., Cuzzi, J.N., Salo, H.J., Danos, R., 2005. HST Observations of spokes in saturn's b ring. *Icarus* 173, 508–521.
- McKay, D.S., Bogard, D.D., Morris, R.V., Korotev, R.L., Johnson, P., Wentworth, S.J., 1986. Apollo 16 regolith breccias: characterization and evidence of early formation in the mega-regolith. *J. Geophys. Res.* 91, D277–D304.
- Mishchenko, M., 2014. *Electromagnetic Scattering by Particles and Particle Groups: An Introduction*. Cambridge University Press.
- Mishchenko, M.I., 1992. The angular width of the coherent back-scatter opposition effect - an application to icy outer planet satellites. *Astrophys. Space Sci.* 194, 327–333.
- Mishchenko, M.I., 1993. On the nature of the polarization opposition effect exhibited by saturn's rings. *Astrophys. J.* 411, 351–361.
- Mishchenko, M.I., Dlugach, J.M., 2009. Radar polarimetry of saturn's rings: modeling ring particles as fractal aggregates built of small ice monomers. *J. Quant. Spectrosc. Radiat. Transf.* 110, 1706–1712.
- Mishchenko, M.I., Dlugach, J.M., 2012. Adhesion of mineral and soot aerosols can strongly affect their scattering and absorption properties. *Opt. Lett.* 37, 704.
- Mishchenko, M.I., Dlugach, J.M., Liu, L., Rosenbush, V.K., Kiselev, N.N., Shkuratov, Y.G., 2009. Direct solutions of the maxwell equations explain opposition phenomena observed for high-albedo solar system objects. *Astrophys. J. Lett.* 705, L118–L122.
- Mishchenko, M.I., Dlugach, J.M., Yurkin, M.A., Bi, L., Cairns, B., Liu, L., Panetta, R.L., Travis, L.D., Yang, P., Zakharova, N.T., 2016. First-principles modeling of electromagnetic scattering by discrete and discretely heterogeneous random media. *Phys. Rep.* 632, 1–75.
- Mishchenko, M.I., Dlugach, Z.M., 1992. The amplitude of the opposition effect due to weak localization of photons in discrete disordered media. *Astrophys. Space Sci.* 189, 151–154.
- Mishchenko, M.I., Rosenbush, V.K., Kiselev, N.N., 2006. Weak localization of electromagnetic waves and opposition phenomena exhibited by high-albedo atmosphereless solar system objects. *Appl. Opt.* 45, 4459–4463.
- Mitchell, C.J., Porco, C.C., Dones, H.L., Spitale, J.N., 2013. The behavior of spokes in saturn's b ring. *Icarus* 225, 446–474.
- Morishima, R., Spilker, L., Brooks, S., Deau, E., Pilorz, S., 2016. Incomplete cooling down of saturn's a ring at solar equinox: implication for seasonal thermal inertia and internal structure of ring particles. *Icarus* 279, 2–19.
- Muinonen, K., 1990. *Light Scattering by Inhomogeneous Media: Backward Enhancement and Reversal of Linear Polarization*. University of Helsinki, Finland.
- Muinonen, K., 1994. Coherent backscattering by solar system dust particles. In: Milani, A., di Martino, M., Cellino, A. (Eds.), *Asteroids, Comets, Meteors 1993*. Vol. 160 of *IAU Symposium*, pp. 271–296.
- Muinonen, K., Mishchenko, M.I., Dlugach, J.M., Zubko, E., Penttilä, A., Videen, G., 2012. Coherent backscattering verified numerically for a finite volume of spherical particles. *Astrophys. J.* 760, 118.
- Müller, G., 1885. Resultate aus helligkeitsmessungen des planeten saturn. *Astron. Nachr.* 110, 225–232.
- Müller, G., 1893. Helligkeitsbestimmungen der grossen planeten und einiger asteroiden. *Publikationen des Astrophysikalischen Observatoriums zu Potsdam* 30, 198–389.
- Nelson, R.M., Hapke, B., Brown, R.H., Spilker, L.J., Smythe, W.D., Kamp, L., Borryta, M.C., Leader, F., Matson, D.L., Edgington, S., Nicholson, P.D., Filacchione, G., Clark, R.N., Bibring, J.-P., Baines, K.H., Buratti, B.J., Bellucci, G., Capaccioni, F., Ceroni, P., Combes, M., Coradini, A., Cruikshank, D.P., Drossart, P., Formisano, V., Jaumann, R., Langevin, Y., McCord, T.B., Mennella, V., Sicardy, B., Sotin, C., 2006. Cassini observations of the opposition effect of saturn's rings-1. In: Mackwell, S., Stansbery, E. (Eds.), *37th Annual Lunar and Planetary Science Conference*, Vol. 37, p. #1461.
- Nelson, R.M., Hapke, B., Smythe, W.D., Spilker, L.J., 2000. The opposition effect in simulated planetary regoliths. reflectance and circular polarization ratio change at small phase angle. *Icarus* 147, 545–558.
- Nicholson, P.D., Hedman, M.M., Clark, R.N., Showalter, M.R., Cruikshank, D.P., Cuzzi, J.N., Filacchione, G., Capaccioni, F., Ceroni, P., Hansen, G.B., Sicardy, B., Drossart, P., Brown, R.H., Buratti, B.J., Baines, K.H., Coradini, A., 2008. A close look at saturn's rings with cassini VIMS. *Icarus* 193, 182–212.
- Noble, S.K., Pieters, C.M., Keller, L.P., 2007. An experimental approach to understanding the optical effects of space weathering. *Icarus* 192, 629–642.
- Ordal, M.A., Bell, R.J., Alexander, R.W., Newquist, L.A., Querry, M.R., 1988. Optical properties of al, fe, ti, ta, w, and mo at submillimeter wavelengths. *Appl. Opt.* 27 (6), 1203–1209.
- Pang, K.D., Voge, C.C., Rhoads, J.W., Ajello, J.M., 1983. Saturn's e-ring and satellite enceladus. In: *Lunar and Planetary Institute Conference Abstracts*, 14, pp. 592–593.
- Parviainen, H., Muinonen, K., 2007. Rough-surface shadowing of self-affine random rough surfaces. *J. Quant. Spectrosc. Radiat. Transf.* 106, 398–416.
- Parviainen, H., Muinonen, K., 2009. Bidirectional reflectance of rough particulate media: ray-tracing solution. *J. Quant. Spectrosc. Radiat. Transf.* 110, 1418–1440.
- Petrova, E.V., Tishkovets, V.P., Jockers, K., 2007. Modeling of opposition effects with ensembles of clusters: interplay of various scattering mechanisms. *Icarus* 188, 233–245.
- Petrova, E.V., Tishkovets, V.P., Jockers, K., 2008. Rebuttal to comment on modeling of opposition effects with ensembles of clusters: interplay of various scattering mechanisms by elena v. petrova, victor p. tishkovets, klaus jockers, 2007 [icarus 188, 233.245]. *Icarus* 194, 853–856.
- Piatek, J.L., Hapke, B., Nelson, R.M., Smythe, W.D., Hale, A.S., 2004. Scattering properties of planetary regolith analogs. *Icarus* 171, 531–545.
- Pieters, C.M., Taylor, L.A., Noble, S.K., Keller, L.P., Hapke, B., Morris, R.V., Allen, C.C., McKay, D.S., Wentworth, S., 2000. Space weathering on airless bodies: resolving a mystery with lunar samples. *Meteorit. Planet. Sci.* 35, 1101–1107.
- Pollack, J.B., Hollenbach, D., Beckwith, S., Simonelli, D.P., Roush, T., Fong, W., 1994. Composition and radiative properties of grains in molecular clouds and accretion disks. *Astrophys. J.* 421, 615–639.
- Porco, C.C., Weiss, J.W., Richardson, D.C., Dones, L., Quinn, T., Throop, H., 2008. Simulations of the dynamical and light-scattering behavior of saturn's rings and the derivation of ring particle and disk properties. *Astron. J.* 136, 2172–2200.
- Poulet, F., Cruikshank, D.P., Cuzzi, J.N., Roush, T.L., French, R.G., 2003. Compositions of saturn's rings a, b, and c from high resolution near-infrared spectroscopic observations. *Astron. Astrophys.* 412, 305–316.
- Poulet, F., Cuzzi, J.N., 2002. The composition of saturn's rings. *Icarus* 160, 350–358.
- Poulet, F., Cuzzi, J.N., French, R.G., Dones, L., 2002. A study of saturn's ring phase curves from HST observations. *Icarus* 158, 224–248.
- Rosenbush, V.K., Avramchuk, V.V., Rosenbush, A.E., Mishchenko, M.I., 1997. Polarization properties of the galilean satellites of jupiter: observations and preliminary analysis. *Astrophys. J.* 487, 402–414.
- Rouleau, F., Martin, P.G., 1991. Shape and clustering effects on the optical properties of amorphous carbon. *Astrophys. J.* 377, 526–540.
- Salo, H., French, R.G., 2010. The opposition and tilt effects of saturn's rings from HST observations. *Icarus* 210, 785–816.
- Salo, H., Karjalainen, R., 2003. Photometric modeling of saturn's rings i. monte carlo method and the effect of nonzero volume filling factor. *Icarus* 164, 428–460.
- Schmidt, J., Ohtsuki, K., Rappaport, N., Salo, H., Spahn, F., 2009. *Dynamics of Saturn's Dense Rings*. Springer, pp. 413–458.
- Seeliger, H., 1884. Zur photometrie des saturnrings. *Astron. Nachr.* 109, 305–314.
- Seeliger, H., 1887. Zur theorie der beleuchtung der grossen planeten insbesondere des saturn. *Abhandl. Bayer. Akad. Wiss. Math.-Naturw. Kl.* 16, 405–516.
- Shevchenko, V.G., Belskaya, I.N., Slyusarev, I.G., Krugly, Y.N., Chiorny, V.G., Gaftonyuk, N.M., Donchev, Z., Ivanova, V., Ibrahimov, M.A., Ehgamberdiev, S.A., Molotov, I.E., 2012. Opposition effect of trojan asteroids. *Icarus* 217, 202–208.
- Shimaki, Y., Arakawa, M., 2012. Low-velocity collisions between centimeter-sized snowballs: porosity dependence of coefficient of restitution for ice aggregates analogues in the solar system. *Icarus* 221, 310–319.
- Shkuratov, Y., Starukhina, L., Hoffmann, H., Arnold, G., 1999. A model of spectral albedo of particulate surfaces: implications for optical properties of the moon. *Icarus* 137, 235–246.
- Shkuratov, Y.G., Bondarenko, S., Kaydash, V., Videen, G., Muñoz, O., Volten, H., 2007. Photometry and polarimetry of particulate surfaces and aerosol particles over a wide range of phase angles. *J. Quant. Spectrosc. Radiat. Transf.* 106, 487–508.
- Shkuratov, Y.G., Kreslavsky, M.A., Ovcharenko, A.A., Stankevich, D.G., Zubko, E.S., Pieters, C., Arnold, G., 1999. Opposition effect from clementine data and mechanisms of backscatter. *Icarus* 141, 132–155.
- Shkuratov, Y.G., Ovcharenko, A., Zubko, E., O. Miloslavskaya, K., Muinonen, Piironen, J., Nelson, R., Smythe, W., Rosenbush, V., Helfenstein, P., 2002. The opposition effect and negative polarization of structural analogs for planetary regoliths. *Icarus* 159, 396–416.

- Shkuratov, Y.G., Zubko, E.S., 2008. Comment on modeling of opposition effects with ensembles of clusters: interplay of various scattering mechanisms by elena v. petrova, victor p. tishkovets, klaus jockers, 2007 [icarus 188, 233–245]. *Icarus* 194, 850–852.
- Showalter, M.R., Nicholson, P.D., 1990. Saturn's rings through a microscope - particle size constraints from the voyager PPS scan. *Icarus* 87, 285–306.
- Smith, B.A., Soderblom, L., Beebe, R.F., Boyce, J.M., Briggs, G., Bunker, A., Collins, S.A., Hansen, C., Johnson, T.V., Mitchell, J.L., Terrile, R.J., Carr, M.H., Cook, A.F., Cuzzi, J.N., Pollack, J.B., Danielson, G.E., Ingersoll, A.P., Davies, M.E., Hunt, G.E., Masursky, H., Shoemaker, E.M., Morrison, D., Owen, T., Sagan, C., Veveřka, J., Strom, R., Suomi, V.E., 1981. Encounter with saturn - voyager 1 imaging science results. *Science* 212, 163–191.
- Tishkovets, V.P., Mishchenko, M.I., 2010. Coherent backscattering: conceptions and misconceptions (reply to comments by bruce w. hapke and robert m. nelson). *J. Quant. Spectrosc. Radiat. Transf.* 111, 645–649.
- Tishkovets, V.P., Petrova, E.V., 2013. Coherent backscattering by discrete random media composed of clusters of spherical particles. *J. Quant. Spectrosc. Radiat. Transf.* 127, 192–206.
- Tishkovets, V.P., Petrova, E.V., 2017. Reflectance model for densely packed media: estimates of the surface properties of the high-albedo satellites of saturn. *Sol. Syst. Res.* 51, 277–293.
- Tishkovets, V.P., Petrova, E.V., Mishchenko, M.I., 2011. Scattering of electromagnetic waves by ensembles of particles and discrete random media. *J. Quant. Spectrosc. Radiat. Transf.* 112 (13), 2095–2127.
- Tuzzolino, A.J., Economou, T.E., Clark, B.C., Tsou, P., Brownlee, D.E., Green, S.F., McDonnell, J.A.M., McBride, N., Colwell, M.T.S.H., 2004. Dust measurements in the coma of comet 81p/wild 2 by the dust flux monitor instrument. *Science* 304, 1776–1780.
- Verbisser, A., French, R., Showalter, M., Helfenstein, P., 2007. Enceladus: cosmic graffiti artist caught in the act. *Science* 315, 815.
- Wallis, B.D., Pilorz, S., Spilker, L.J., Altobelli, N., Brooks, S.M., Edgington, S.G., 2006. CIRS observations of a thermal enhancement near zero phase in saturn's rings. In: AAS/Division for Planetary Sciences Meeting Abstracts #38. Vol. 38 of Bulletin of the American Astronomical Society, p. 561.
- Wallis, B.D., Spilker, L.J., Pilorz, S.H., Pearl, J.C., Altobelli, N., Edgington, S.G., Flasar, F.M., 2005. CIRS Observations of a thermal enhancement near zero phase in saturn's rings. In: AGU Fall Meeting Abstracts, p. B250. CIRS Team.
- Warren, S.G., 1984. Optical constants of ice from the ultraviolet to the microwave. *Appl. Opt.* 23, 1206–1225.
- Warren, S.G., Brandt, R.E., 2008. Optical constants of ice from the ultraviolet to the microwave: a revised compilation. *J. Geophys. Res. (Atmosp.)* 113, D14220.
- Warren, S.G., Brandt, R.E., Grenfell, T.C., 2006. Visible and near-ultraviolet absorption spectrum of ice from transmission of solar radiation into snow. *Appl. Opt.* 45, 5320–5334.
- Wisdom, J., Tremaine, S., 1988. Local simulations of planetary rings. *Astron. J.* 95, 925–940.
- Wolf, P.-E., Maret, G., 1985. Weak localization and coherent backscattering of photons in disordered media. *Phys. Rev. Lett.* 55, 2696–2699.
- Zebker, H.A., Marouf, E.A., Tyler, G.L., 1985. Saturn's rings - particle size distributions for thin layer model. *Icarus* 64, 531–548.
- Zubko, E., Muinonen, K., Shkuratov, Y.G., Videen, G., Nousiainen, T., 2007. Scattering of light by roughened gaussian random particles. *J. Quant. Spectrosc. Radiat. Transf.* 106, 604–615.
- Zubko, E., Shkuratov, Y., Mishchenko, M., Videen, G., 2008. Light scattering in a finite multi-particle system. *J. Quant. Spectrosc. Radiat. Transf.* 109, 2195–2206.
- Zubko, V.G., Mennella, V., Colangeli, L., Bussoletti, E., 1996. Optical constants of cosmic carbon analogue grains - i. simulation of clustering by a modified continuous distribution of ellipsoids. *Mon. Not. R. Astron. Soc.* 282, 1321–1329.